Space Weather

RESEARCH ARTICLE
10.1029/2022SW003166

Key Points:

- Geomagnetically induced currents (GICs) are simulated in a hypothetical representation of a low-latitude power transmission network in southern Brazil
- Large GICs are mainly concentrated in the central part of the network, primarily in the E-W transmission lines and low conductance zones
- Simulation results will be used to identify regions more exposed to GIC hazards to guide the installation of GIC sensors in southern Brazil

Correspondence to:
K. V. Espinosa,
karen.sarmiento@inpe.br

Citation:
Espinosa, K. V., Padilha, A. L., Alves, L. R., Schultz, A., & Kelbert, A. (2023). Estimating geomagnetically induced currents in southern Brazil using 3-D Earth resistivity model. *Space Weather*, *21*, e2022SW003166. https://doi.org/10.1029/2022SW003166

Received 26 MAY 2022
Accepted 15 JAN 2023

Estimating Geomagnetically Induced Currents in Southern Brazil Using 3-D Earth Resistivity Model

Karen V. Espinosa[1], Antonio L. Padilha[1], Livia R. Alves[1], Adam Schultz[2], and Anna Kelbert[3]

[1]Instituto Nacional de Pesquisas Espaciais (INPE), São José dos Campos, Brazil, [2]Oregon State University, Corvallis, OR, USA, [3]U.S. Geological Survey, Geomagnetism Program, Golden, CO, USA

Abstract Geomagnetically induced currents (GICs) result from the interaction of the time variation of ground magnetic field during a geomagnetic disturbance with the Earth's deep electrical resistivity structure. In this study, we simulate induced GICs in a hypothetical representation of a low-latitude power transmission network located mainly over the large Paleozoic Paraná basin (PB) in southern Brazil. Two intense geomagnetic storms in June and December 2015 are chosen and geoelectric fields are calculated by convolving a three-dimensional (3-D) Earth resistivity model with recorded geomagnetic variations. The dB/dt proxy often used to characterize GIC activity fails during the June storm mainly due to the relationship of the instantaneous geoelectric field to previous magnetic field values. Precise resistances of network components are unknown, so assumptions are made for calculating GIC flows from the derived geoelectric field. The largest GICs are modeled in regions of low conductance in the 3-D resistivity model, concentrated in an isolated substation at the northern edge of the network and in a cluster of substations in its central part where the east-west (E-W) oriented transmission lines coincide with the orientation of the instantaneous geoelectric field. The maximum magnitude of the modeled GIC was obtained during the main phase of the June storm, modeled at a northern substation, while the lowest magnitudes were found over prominent crustal anomalies along the PB axis and bordering the continental margin. The simulation results will be used to prospect the optimal substations for installation of GIC monitoring equipment.

Plain Language Summary The Sun is a source of explosive space weather events in which large amounts of radiation and atomic particles are released in short periods of time. When these bursts of energy impact the Earth's environment, electrical current systems in the magnetosphere and ionosphere are affected, giving rise to large variations in the geomagnetic field called magnetic storms. The rate of change in the geomagnetic field during magnetic storms induces geoelectric fields in the Earth's subsurface. These geoelectric fields can drive hazardous quasi-direct geomagnetically induced currents (GICs) to flow in large-scale grounded technological systems such as power grids, railways, or oil and gas pipelines. Large GIC events most often occur at high latitudes in the vicinity of dynamic ionospheric current systems. However, long transmission lines built recently over greater distances and induction effects amplifying ground-level electric fields in regions of complex Earth structure make power grids more exposed to GIC flows, even at low latitudes. In this study, we simulate the GICs produced during geomagnetic storms in a low-latitude electrical grid in southern Brazil. A cluster of substations with potential risk of larger GICs has been identified in the network and will be the focus of mitigation strategies and quantitative monitoring.

1. Introduction

Geomagnetic storms occur when solar activity increases and solar wind interacts with the Earth's magnetic field. This interaction can result in rapid changes in the geomagnetic field and induce geoelectric fields at the Earth's surface and interior, according to Faraday's law of electromagnetic (EM) induction. The geoelectric fields drive currents in the ground through power systems, pipelines, and other electrically earthed technological systems. The frequency of the current is substantially lower than the operational frequency of electric power transmission grids; therefore, it is considered quasi-direct current (DC) and is commonly known as geomagnetically induced current (GIC; e.g., Boteler, 1994; Pirjola, 2000). GICs can cause substantial damage to pipelines through increased corrosion and can affect power networks through premature aging of transformers (Pirjola et al., 2000).

Larger GICs (100 to −500 A, Viljanen et al., 2013) observed at high latitudes have been attributed to amplification by intense ionospheric current systems in the vicinity of auroral ovals (Pirjola, 2000). However, as a result of the increasing interconnection between isolated national power grids and induction effects associated with complex three-dimensional (3-D) geoelectric structure along transmission line paths, several problems caused by these currents during intense magnetic storms have also been reported at low and mid geomagnetic latitudes (Gaunt & Coetzee, 2007; Marshall et al., 2012). Specifically in the low latitudes of South America, GICs with amplitudes up to a few tens of amperes have been measured/modeled during geomagnetically active periods in Brazil (Barbosa, Alves, et al., 2015; Espinosa et al., 2019; Trivedi et al., 2007) and Uruguay (Caraballo et al., 2013).

GICs can be directly measured using a Hall effect probe installed at the ground neutral of substations in a power network (e.g., Marshall et al., 2013; Torta et al., 2012). However, installing a sensor for GIC measurements in a high-power substation involves a lengthy discussion with transmission line operators. Alternatively, GICs can be modeled by estimating horizontal geoelectric fields in the region of interest, by combining geomagnetic time series with a ground resistivity model, and then calculating the GICs triggered by these geoelectric fields in the power grid using information about its electrical configuration, geometry, and resistances (Pirjola, 2000). In South America, direct measurements of GICs using a Hall sensor were available for the period 2009–2014 at a substation in central Brazil (Barbosa, Alves, et al., 2015). All other studies were based on indirect estimates, using magnetic field measurements available at the Earth's surface, modeling the geoelectric field based on some knowledge of ground resistivity, and calculating GIC from the topology and electrical parameters of the electric power grid. These studies used very simple one-dimensional (1-D) layered models to represent the Earth's resistivity and a 1 min cadence for the geomagnetic field time series allowing to estimate the geoelectric field also with a 1 min cadence. However, a plethora of recent scientific reports have shown that the use of local 1-D models may result in large errors in the estimated geoelectric field amplitudes (in some cases exceeding two orders of magnitude) when compared to results derived from more realistic 3-D resistivity models (e.g., Bedrosian & Love, 2015; Bonner & Schultz, 2017; Cuttler et al., 2018; Kelbert & Lucas, 2020; Lucas et al., 2018; Sun & Balch, 2019; Weigel, 2017). Also, other studies have shown that modeling with a magnetic field sampling period of 1 min underestimates the peaks of the surface geoelectric field because the high-frequency spectral content of the geomagnetic field is neglected (Gannon et al., 2017; Grawe et al., 2018; Pulkkinen et al., 2006). However, limitations in the magnetotelluric (MT) and geomagnetic deep sounding (GDS) data used to derive the 3-D impedance tensors in the study area did not allow us to use the full potential of having geomagnetic variations with an acquisition rate of 1 s to calculate the geoelectric field.

In this paper, we present the first GIC study in a South American power grid using 3-D subsurface resistivity structure and high-cadence geomagnetic variations to derive geoelectric fields during geomagnetic storms. One-second geomagnetic data from the Brazilian space weather magnetometer network (EMBRACE program; Denardini et al., 2018) were interpolated across southern Brazil using the spherical elementary current system method (SECS, Amm & Viljanen, 1999) for two geomagnetic storms. Following the plane-wave MT assumption, the interpolated geomagnetic data were convolved with 3-D MT impedances derived from forward calculation of a new Earth resistivity model for the study region to obtain the surface geoelectric fields. Finally, a model of the southern Brazil 525 kV transmission grid was combined with the calculated geoelectric fields, and resultant GICs were computed at the nodes (substations) of the grid (Lehtinen & Pirjola, 1985). The main goals of this simulation are to implement an operational methodology for the EMBRACE program to assess potential GIC hazards in the Brazilian power transmission system and locate weak spots in the analyzed grid, more susceptible to the risk derived from induced currents. At these critical sites, GIC sensors are planned to be installed for further validation efforts.

2. Theoretical Background

Transient structures from the Sun, principally coronal mass ejections (CMEs), travel through the interplanetary environment and may cause a drastic response from the magnetosphere. During geoeffective events, the current systems in the magnetosphere and ionosphere are intensified, being perceived as time-variations in the magnetic field on the Earth's surface, according to Ampere's law. Throughout geomagnetically disturbed periods, the electromagnetic signal that propagates in all directions reaches the surface of the Earth, with only a small proportion penetrating its interior. An electric field will be induced in the subsurface, as a function of the temporal rate of change of the geomagnetic field and the time-invariant, to first order, electrical resistivity structure inside the Earth. The induction and diffusion of this electric field within the Earth depend on the subsurface electrical resistivity structure ρ (or its reciprocal conductivity σ). Thus, the induced geoelectric field (E) conducts electrical currents (J) implicitly expressed in the constitutive relation $J = \sigma E$.

Grounded power transmission lines form a closed path with Earth's subsurface. An electromotive force is induced through this loop and acts as an external voltage source. The induced geoelectric field has the same amplitude and direction as the electric field along the voltage lines and is responsible for the GICs along the long lines integrating the power network (Boteler & Pirjola, 2017). In the chain of processes involved in the occurrence of GICs, it is observed that the amplitude of the induced geoelectric field does not only depend on the geomagnetic disturbance (storms or sub-storms), but also on the distribution of resistivity (ρ) on subsurface and on the characteristics and configuration of the electrical network. Following Pirjola (2002), GIC modeling process can be divided into: (a) the geophysical problem for obtaining the geoelectric field, in this case, from a 3-D resistivity model and (b) the engineering approach using the Lehtinen-Pirjola (LP) method.

2.1. SECS Interpolation Method

The variations of the geomagnetic field in the study region were obtained using the SECS interpolation technique, using the Cartesian Elementary Current Systems (CECS) variant defined for a Cartesian geometry (Vanhamäki & Juusola, 2020). SECS interpolating method is a physics-inspired technique for obtaining variations of the geomagnetic field on the surface as a function of an equivalent currents system in the ionosphere (Amm, 1997; Amm & Viljanen, 1999).

In this method, any ionospheric current density $J(r)$ can be described as a sum of its curl-free J_{cf} and divergence-free J_{df} components. Here, J_{cf} do not produce any magnetic field below the ionosphere because the sum of the currents associated with the field-aligned currents (FACs), assumed to flow radially upward or downward in the ionosphere, will nearly cancel each other out. Thus, the total ionospheric current is assumed to be produced exclusively by the divergence-free part (J_{df}), which is described by the equivalent current density capable of producing the same effect in the continuation of the disturbance of the magnetic field below the ionosphere (Bernhardi et al., 2008). Of note, only external sources are being considered, with internal telluric sources being neglected.

In a planar geometry where the Earth's curvature is neglected, the horizontal magnetic field due to an elementary ionospheric current with current amplitude I, at height h above the Earth's surface, in cylindrical coordinates is given by:

$$B(\rho) = \frac{\mu_0 I}{2\pi\rho}\left(1 - \frac{h}{\sqrt{\rho^2 + h^2}}\right)\vec{e}_\rho \tag{1}$$

where μ_0 is the permeability of free space, $\rho = \sqrt{x^2 + y^2}$ is the radial distance from the current element at the ionosphere to the field point over the x, y-plane (here defined as the Earth's surface), and $\vec{e}_\rho$ is the unit vector in the ρ-direction. The amplitude of the current elements can be calculated by fitting the modeled horizontal geomagnetic field associated with the ionospheric elementary currents to the geomagnetic field measured at ground stations:

$$\begin{bmatrix} B_j(x_i, y_i) \\ . \\ . \\ B_j(x_N, y_N) \end{bmatrix} = \begin{bmatrix} M_{j,11} & \dots & M_{j,1K} \\ . & & . \\ . & & . \\ M_{j,N1} & \dots & M_{j,NK} \end{bmatrix} \begin{bmatrix} I_1 \\ . \\ . \\ I_K \end{bmatrix} \tag{2}$$

where the left-hand side matrix $B_{j,(x,y)}$ is the measured geomagnetic field, the right-hand side matrix $M_{j,NK}$ is composed by geometrically proportionally factors and the vector $\boldsymbol{I}_K$ represents the amplitude of the equivalent current at each pole (Bernhardi et al., 2008). This system is generally underdetermined because the number of measurements is much less than the number of elementary currents and therefore must be solved by singular value decomposition (Pulkkinen et al., 2003).

2.2. Geoelectric Field Estimation

Geoelectric fields are estimated by applying basic electromagnetic induction equations to the Earth's current system (Chave & Jones, 2012; Simpson & Bahr, 2005). Assuming plane wave (i.e., spatially uniform) fields excited far above the Earth's surface and neglecting displacement currents, the tensor relationship between the frequency-dependent horizontal components of the geomagnetic (B) and the induced geoelectric (E) fields through the impedance transfer function (Z) of the MT method can be used:

$$\begin{pmatrix} E_x(\omega) \\ E_y(\omega) \end{pmatrix} = \frac{1}{\mu_0}\begin{bmatrix} Z_{xx}(\omega) & Z_{xy}(\omega) \\ Z_{yx}(\omega) & Z_{yy}(\omega) \end{bmatrix}\begin{pmatrix} B_x(\omega) \\ B_y(\omega) \end{pmatrix} \tag{3}$$

where ω is the angular frequency and x and y denote orthogonal directions in the horizontal plane at the Earth's surface. The assumption of the inducing field as a plane-wave is an approximation of a special case of EM induction, in which the spatial non-uniformity of the inducing field can be neglected (Utada, 2018). This traditional interpretation of the electromagnetic response functions implies that the spatial wavelength of the inducing source field is large compared to its diffusion length (skin depth) into the subsurface, which is generally valid in low and middle latitudes, where the main source of anomalous geomagnetic disturbances is a large-scale magnetospheric ring current (Marshalko et al., 2021). The complex-value impedance tensor depends on the local geological structure, which varies as a function of rock composition, including the physical, chemical, and thermal state. For a stable tectonic environment, such as the study region, impedances are stationary functions for the periods relevant to GIC.

These impedances can be derived from electrical resistivity models and used to approximate geoelectric fields at locations where the geomagnetic fields are available during a magnetic storm. As the geomagnetic field is in the time domain and the impedance tensor is in the frequency domain, Fourier transformation is required to obtain the geomagnetic field in the frequency domain. Then, the components of the induced geoelectric field are estimated in the frequency domain using Equation 3. Finally, the inverse Fourier transform is used to obtain the horizontal components of the time series of the geoelectric field.

2.3. GIC Modeling

Because the variation of the induced geoelectric field is rather slow, GICs can be approximated as quasi-direct currents (frequency ranges of decihertz or lower) superimposed on the 50/60 Hz power system currents. The induced geoelectric field can be represented by a voltage source between two substations (e.g., i and j) of a transmission line. This voltage can be calculated by integrating the vector electric field along the length between the substations and expressed as:

$$V_{ji} = \int_C \vec{E}\,dl = \int_i^j \vec{E}\,dl \tag{4}$$

where the line integral is along each finite segment of the path C between substations i and j, which takes into account the amplitude and direction of the electric field $\left(\vec{E}\right)$, V_{ji} represents the voltage source between substations i and j, and dl represents the incremental length of the line.

Following Kirchhoff's laws, Lehtinen and Pirjola (1985) proposed an approach (LP method) to calculate earthing currents flowing in or out of the system at substation locations. In this case, the network is considered as a set of discrete grounded nodes, connected by the transmission line through a path ($i - j$). Using this method, the GIC flow through n earthed substations can be calculated as

$$I_n = (U + YZ_n)^{-1}J_n \tag{5}$$

where I_n is a $n \times 1$ vector of GICs flowing into the Earth, U is the $n \times n$ unit matrix, Y represents a $n \times n$ network admittance matrix that mainly depends on the resistance of the conductors, Z_n represents a $n \times n$ matrix containing earthing impedance, and J_n is a $n \times 1$ column vector with the induced nodal current sources. The elements of the nodal admittance matrix Y are defined by the resistance per unit length of the transmission lines (R_{ij}) interconnecting the substations, which are represented by

$$Y_{ij} = \frac{-1}{R_{ij}} \qquad i \neq j \qquad Y_{ij} = \sum_{\substack{k=1 \\ i\neq k}}^{n} \frac{1}{R_{ij}} \qquad i = j \tag{6}$$

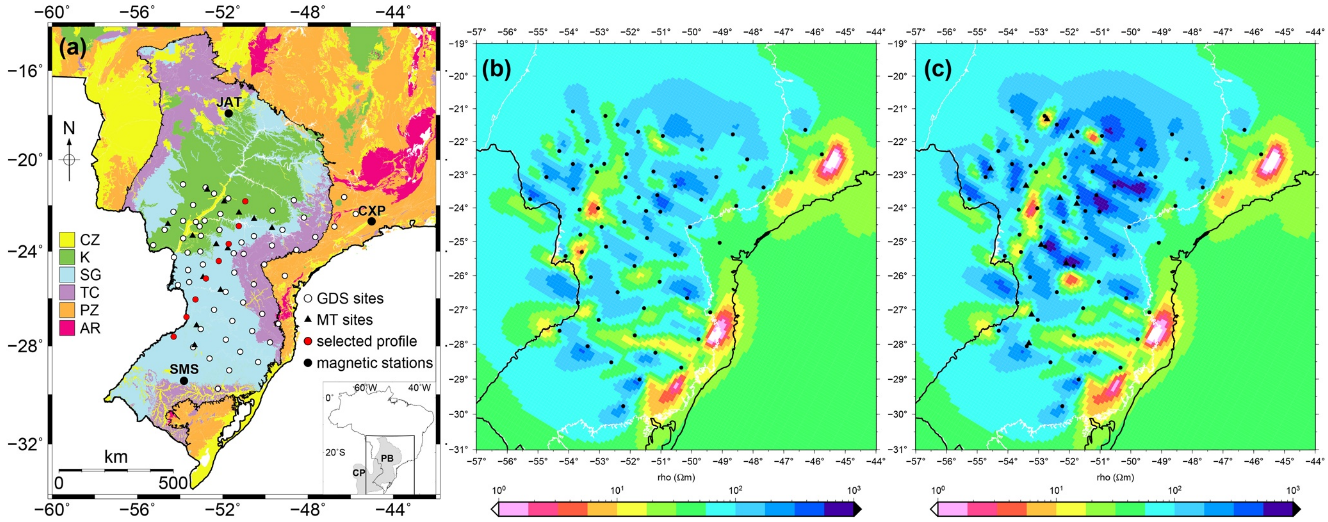

Figure 1. Regional geology and 3-D resistivity models for the study area. (a) Generalized geological map of southern Brazil, with emphasis on the Brazilian part of the Paraná basin (PB) (modified from Bizzi et al. (2001)). Locations of geomagnetic deep sounding (GDS), long-period magnetotelluric (MT) and EMBRACE magnetic stations are shown. Geological periods of outcrops are: CZ = Cenozoic; K = Cretaceous sediments; SG = Early Cretaceous basalts; TC = Triassic to Cambrian sediments; PZ = Proterozoic; and AR = Archean. The inset shows the study area with the full areal extent of the PB and contiguous Chaco-Paraná basin in northeastern Argentina. (b) A horizontal section at depth of 33 km from the 3-D resistivity model of Padilha et al. (2015), derived from GDS data alone. Position of the GDS sites (dots) and PB boundaries (white dashed lines) is shown. (c) Same as (b) from the 3-D resistivity model derived for this study using joint GDS (dots) and long-period MT (triangles) data.

Also, based on the calculated voltage using Equation 4, the elements of the column matrix J_n can be obtained through

$$J_{ni} = \sum_{j \neq i} \frac{V_{ji}}{R_{ji}} \tag{7}$$

3. Data Sources

As previously described, simulating GICs on a power grid during a magnetic storm requires knowledge of the Earth's resistivity structure, magnetic field observations, and a representation of the high voltage transmission system, including information about its topology, network resistances, and locations of substation grounding points. The following information is available for southern Brazil to calculate GIC flows during the 2015 geomagnetic storms.

3.1. Available Geological and Geoelectrical Information

The study area in south-central Brazil is positioned on the tectonically stable part of the South American platform. This is characterized by a central core formed by several Archean to Mesoproterozoic cratonic nuclei from earlier supercontinents welded together during the Neoproterozoic Brasiliano/Pan African orogeny in the final assembly of West Gondwana (Almeida et al., 2000). A very wide segment of this Precambrian framework is covered by intracratonic basins.

South-central Brazil (Figure 1a) is marked by the presence of the Paraná basin (PB), a large intracratonic feature deposited from Late Ordovician to Late Cretaceous in response to a geological stabilization after the Brasiliano orogeny. The basin comprises a thick and extensive sedimentary-magmatic sequence, which covers an area of approximately 1,700,000 km^2, mainly in southern Brazil, but also in Uruguay, Paraguay, and Argentina. Its stratigraphic succession outlines successive episodes of subsidence and uplift, with a thickness of up to 7,000 m in the central depocenter (Zalán et al., 1990). Just prior to the breakup of the supercontinent Pangaea in the Early Cretaceous, one of the most voluminous volcanic events in the Earth's history covered the basin with basaltic lava flows, while many dykes and sills also intruded the sedimentary sequence (Melfi et al., 1988). After basaltic volcanism, the northern part of the basin subsided and a thin layer of continental sediments was deposited in the

Table 1
Geographic and Geomagnetic Coordinates and Total Geomagnetic Field Strength at the Selected EMBRACE Stations for the Year 2015

	Geographic		Geomagnetic			
Station code	Latitude	Longitude	Latitude	Longitude	Total field (nT)	Inclination (°)
CXP	22.70°S	45.01°W	19.49°S	22.41°E	23,085	−37.56
JAT	17.93°S	51.72°W	12.61°S	17.77°E	23,024	−25.37
SMS	29.44°S	53.82°W	21.62°S	13.50°E	22,477	−37.18

Late Cretaceous, ending the depositional history of the basin. Below the basin, the basement structure remains uncertain with different proposed lithospheric models, such as a single cratonic block underneath the basin axial region surrounded by mobile belts of Brasiliano age (Mantovani et al., 2005) or a collage of fragmented blocks separated by interposed suture zones (Milani & Ramos, 1998). Padilha et al. (2015) provide additional extensive information on the geological setting of the PB.

The 3-D deep electrical resistivity structure of this region was previously investigated using the same 63 regional-scale GDS data with an average site interval of ~100 km (see GDS station distribution in Figure 1a), but constrained by different MT data sets (Maurya et al., 2018; Padilha et al., 2015). These MT data were mainly from broadband soundings positioned along profiles in the central part of the basin. The two studies generically modeled the same resistivity distribution at medium-to-lower crustal and upper mantle depths, which are represented in Figure 1b through a horizontal resistivity map at a lower crustal depth (33 km) of the model by Padilha et al. (2015). It shows that the crust below the basin consists of several quasi-linear highly conducting channels of limited lateral extent. It has been proposed by these authors that the conductors represent signatures of ancient crustal/lithospheric discontinuities, reactivated during flood volcanism. These weakness zones acted as the main area for basalt extrusion, with the enhanced conductivity associated with the impregnation of iron-enriched fluids during the magmatic activity leaving a conductive solid residue.

A new 3-D resistivity model was derived for this study incorporating 13 long-period MT stations distributed over different regions of the PB to the GDS array data. The parallel inversion code ModEM (Egbert & Kelbert, 2012; Kelbert et al., 2014) was used for data inversion that included all four components of the impedance tensor of the MT sites (periods from 300 to 10,000 s and error floors of 5% for the off-diagonal and 10% for the on-diagonal impedance elements) and tipper responses of GDS and MT sites (periods from 300 to 5,000 s and a constant error floor of 0.02). The model grid was the same as that of Padilha et al. (2015), with a covariance value of 0.3 applied once in all directions and the Atlantic Ocean (0.3 Ωm seawater resistivity) included as a priori and fixed structure. The previous model of Padilha et al. (2015) was used as the starting model, and after 77 iterations the inversion converged to a normalized root mean square of 2.8. The final 3-D inversion model is represented in Figure 1c by a horizontal slice at a depth of 33 km. The same elongated major conductivity anomalies are observed when comparing the previous (Figure 1b) and current (Figure 1c) 3-D resistivity models. However, the new model features a more resistive crustal core, especially in the northern portion of the basin where most long-period MT soundings are concentrated. This new 3-D model will be used here to obtain the geoelectric fields during the chosen geomagnetic storms.

3.2. Geomagnetic Field Variations

Geomagnetic variations recorded by fluxgate magnetometers of the EMBRACE program (see Denardini et al. (2018), for magnetometer characteristics) with 1 s sampling rate were used in this study. Two intense geomagnetic storms that occurred in the decreasing phase of the sunspot cycle 24, on 21–23 June 2015 (minimum Dst of −198 nT) and 19–21 December 2015 (minimum Dst of −166 nT), were chosen for GIC modeling. Of the 16 magnetic stations currently operated in the EMBRACE array, three were selected based on data availability for the two events and geographic distribution around the study region (see Figure 1a). Details on the stations are presented in Table 1, where the geomagnetic information was obtained using the International Geomagnetic Reference Field 13th generation release (IGRF-13) (Alken et al., 2021).

The June storm was associated with an active region on the Sun that produced a sequence of CMEs related to strong flares from 18 to 25 June 2015 (Liu et al., 2015). The geomagnetic disturbances at Earth were caused by

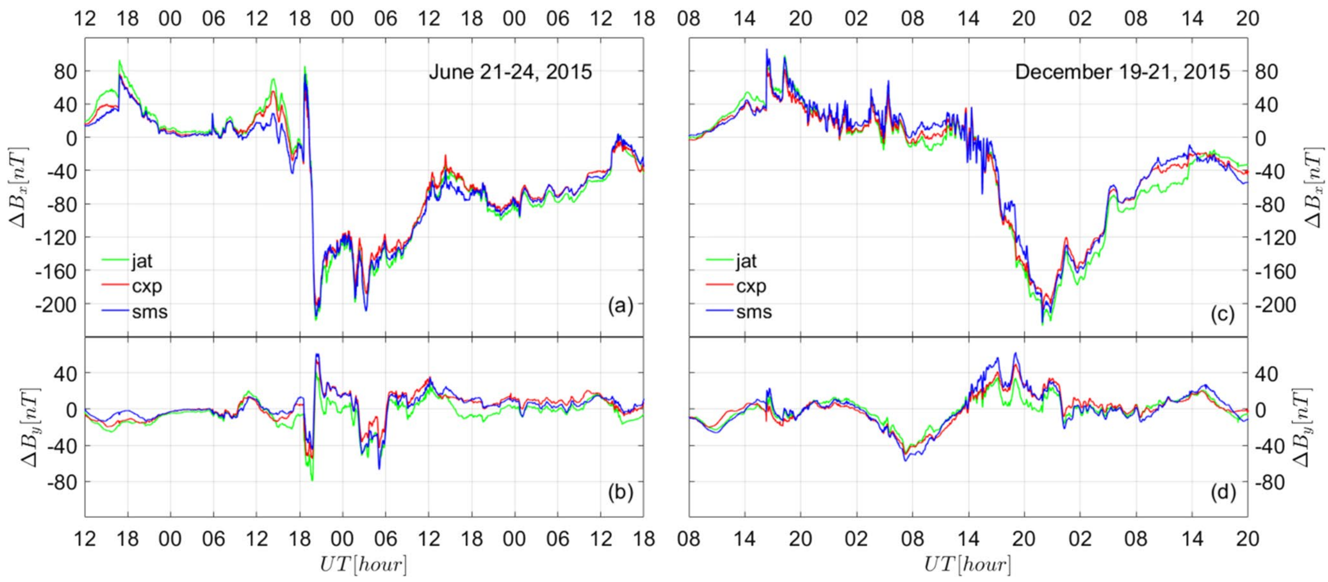

Figure 2. Low-pass filtered geomagnetic field time series with a cutoff frequency of 100 mHz for northward (ΔB_x) and eastward (ΔB_y) components at the three EMBRACE stations during the geomagnetic storms of June (left panels; from 12:00 on 21 June to 18:00 UT on 24 June 2015) and December (right panels; from 08:00 on 19 December to 20:00 UT on 21 December 2015).

three interplanetary shocks that impacted the magnetosphere on 21 June at around 16:49 Universal Time (UT) and on 22 June at around 05:48 and 18:35 UT. The first two shocks produced small spikes in the geomagnetic field, but the third shock was accompanied by a sudden increase in the solar wind speed due to amplification by the preceding shocks and a large southward (B_z) interplanetary magnetic field (IMF) component that triggered a great geomagnetic storm (see Astafyeva et al. (2016), for more details).

The December storm was linked to two asymmetric CMEs that merged in the interplanetary medium and reached Earth on 19 December at ∼16:18 UT. The IMF B_z fluctuated near the zero levels for several hours but suddenly turned south on 20 December around 04:00 UT giving rise to the main phase of the geomagnetic storm, which reached its minimum *Dst* value at ∼22:50 UT of the same day. The southern direction of the IMF B_z had a very long duration, lasting up to ∼15:00 UT on 21 December (see Cherniak and Zakharenkova (2018), for more information).

EMBRACE magnetometers produce digital samples at a rate of one sample per second, which are averaged to 1 min resolution for data distribution (Denardini et al., 2018). Specifically for this study, the 1-s time resolution raw measurements were accessed and the first derivatives of the horizontal (*H*) and declination (*D*) magnetic vector components were used to identify local spikes and other artificial disturbances. A preliminary assessment of the horizontal magnetic field derivative (dH/dt) was thus performed to identify unexpected spikes by comparing the geomagnetic signatures of the three stations during the two geomagnetic storms. Furthermore, a comparison of the power spectrum between the three stations made it possible to identify the natural signals and remove local EM noise from the time series. After that, a low-pass filter with a cutoff frequency of 100 mHz (equivalent period of 10 s) was chosen to remove high-frequency components in the raw magnetic data. This is in line with previous studies arguing that the geomagnetic field variations that generate the greatest risk for high voltage power grid transformers occur in periods of about 10–1,000 s (e.g., Bedrosian & Love, 2015; Cuttler et al., 2018). Following, the filtered *H* and *D* geomagnetic data were converted into northward (B_x) and eastward (B_y) data, using $B_x = H\cos D$ and $B_y = H\sin D$.

The magnetic signature of the two geomagnetic storms is shown in Figure 2, which presents the B_x and B_y components of the horizontal magnetic field at the three EMBRACE stations. As a typical result for low geomagnetic latitudes, the magnetic field variation of the northward component is much greater than that of the eastward component. In addition, the recorded geomagnetic variations are very similar in the three stations, despite the great separation between them (maximum distance of 1,300 km between JAT and SMS) and possible effects that could be ascribed to the South Atlantic Magnetic Anomaly (SAMA). In the latter case, southeastern Brazil is at

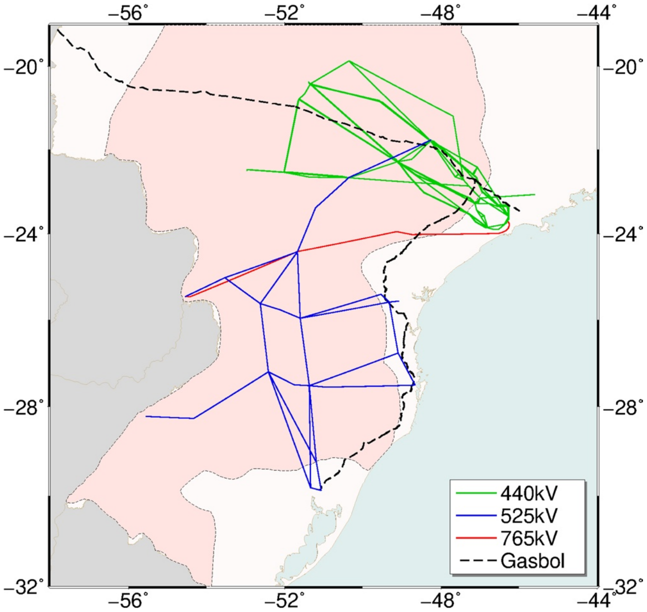

Figure 3. Map with straight-line approximations of the three main high-voltage transmission lines in south-southeast Brazil (ONS, 2022) and the path of the Gasbol pipeline. The region covering the Paraná basin in Brazil is shown in pink.

the center of this anomaly, as seen by the low total field strength values at the three stations in Table 1. This global minimum geomagnetic field intensity leads to enhanced energetic particles precipitation in the local ionosphere as a regular feature, even under magnetically quiet conditions (Paulikas, 1975). Particle precipitation can be further enhanced during magnetically disturbed periods (Abdu et al., 2005), and increased amplitudes in magnetic horizontal components have been reported at the center of SAMA during magnetic storms (Trivedi et al., 2005). However, the ground geomagnetic variations shown in Figure 2 apparently do not indicate that SAMA ionospheric effects contributed substantially during the two analyzed storms.

3.3. High-Voltage Power Transmission Lines of South-Southeast Brazil

Brazil's power system reflects the country's continental dimensions by its extension and complexity. As a result of the continued growth in energy demand, grid topology, determined primarily by hydropower distribution, is becoming increasingly elongated and interconnected. In addition, the density of power lines and substations is uneven due to substantially higher demand in major urban areas.

South-southeast Brazil is the most populous and industrialized region in the country, thus presenting the largest number of high voltage networks and power plants. The high-voltage network in this region consists of transmission lines with a voltage level of up to 765 kV. A simplified representation of the grid is shown in Figure 3, where network branches with different operating voltages are presented with colored lines (red = 765, blue = 525, and green = 440 kV). Lower voltage elements of the power network (mainly 345 and 230 kV) are not included in the figure, which also shows the layout of the Bolivia-Brazil gas pipeline (Gasbol).

For the GIC simulation model, only the 525 kV network was considered because it is located within the region where the 3-D resistivity model is available and the geomagnetic interpolations are more reliable. Lower-level voltage grids were ignored in these calculations as the most intense GICs are expected in the higher-voltage network due to longer line sections and lower line resistances (Zheng et al., 2014). However, several studies have shown that neglecting the lower voltage portion of a network can lead to overestimated GICs (e.g., Blake et al., 2018; Torta et al., 2014), particularly in substations with direct connections to the lower voltage elements. Our modeling is justified because we are at this stage mainly looking for the areas most susceptible to large increases in GIC for monitoring equipment installation, rather than trying to make an accurate GIC prediction. The 525-kV network is composed of 31 transmission lines and 23 substations, each one corresponding to a ground node represented by a simple conductor. This means that a three-phase power transmission line is connected to a transformer with a neutral point into the ground, with the total resistance given by the sum of the transformer resistance and the earthing resistance. In this study, we assumed identical grounded resistances at all grounding points, resulting in a 525-kV hypothetical power network with a realistic geometric coverage of the area.

4. Estimates of Geoelectric Fields During the 2015 Geomagnetic Storms

Along with the 3-D resistivity model for the region encompassing the PB in southern Brazil, the geomagnetic field variations recorded by EMBRACE magnetometers can be used to estimate geoelectric fields during the 2015 storms. The procedure involves an initial interpolation of the magnetic field in the region of interest (as described in Section 2.1) and its subsequent convolution with the impedances from the resistivity model to obtain the geoelectric field (Section 2.2). Computer codes were developed to perform these calculations using the MATLAB platform.

4.1. Interpolating the Geomagnetic Field Variations

The SECS interpolation method has been shown to give good results at high latitudes (Pulkkinen et al., 2003; Rigler et al., 2019; Vanhamäki & Amm, 2011; Weygand et al., 2011), where almost vertical FAC flowing radially along the geomagnetic field and connecting ionospheric currents to the magnetosphere is a reasonable

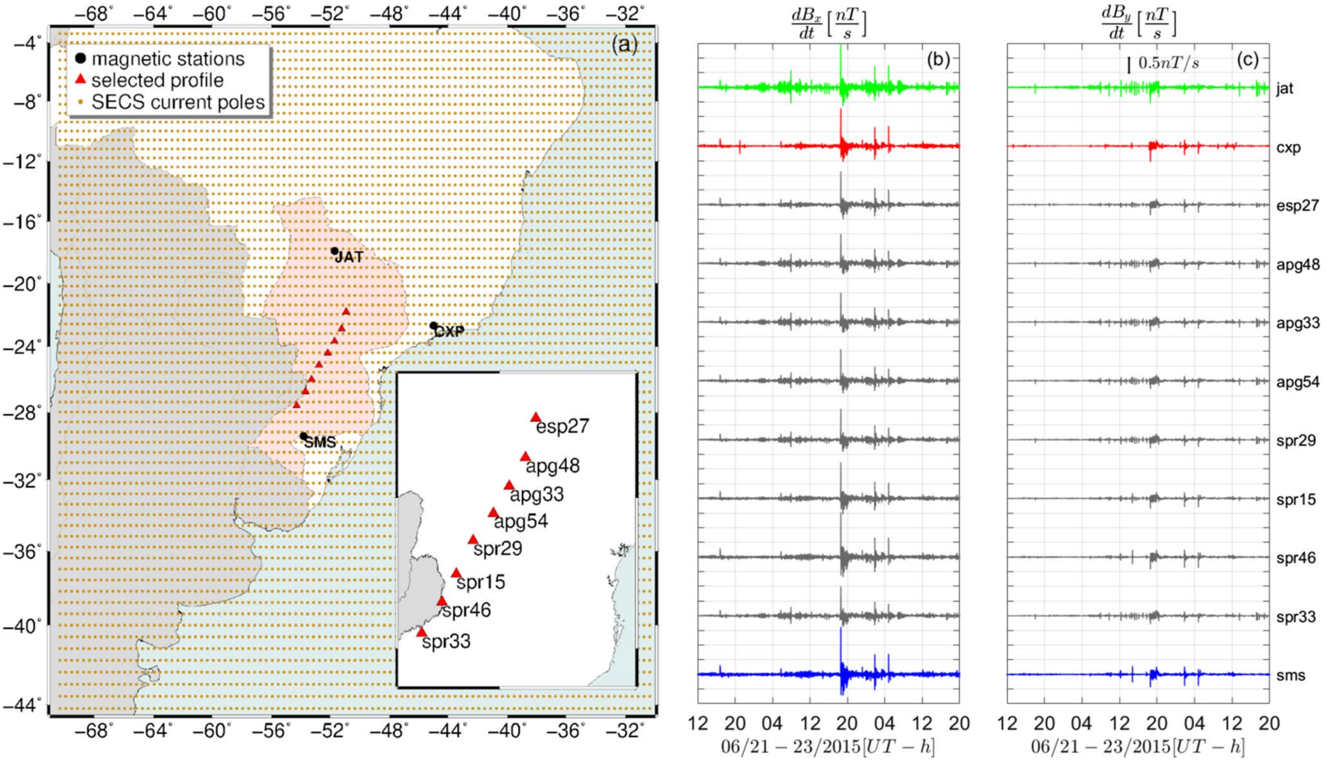

Figure 4. Spherical elementary current system method (SECS) interpolation of geomagnetic field variations. Areal extent of Brazil (white) in the South America region with the Atlantic Ocean in the east Brazilian continental margin and the west-south terrestrial boundaries (gray). The region covering the Paraná basin in Brazil is shown in pink. (a) Equivalent ionospheric current grid (brown dots) to estimate the elementary current amplitudes. Red closed triangles indicate the locations where the SECS amplitudes are calculated on the surface, with the inset showing the geomagnetic deep sounding site names along the chosen profile. (b) dB_x/dt observed at geomagnetic stations (JAT—green, CXP—red, and SMS—blue) and interpolated at the selected profile sites from 12:00 on 21 June to 20:00 UT on 23 June 2015. (c) Same as (b) for dB_y/dt.

approximation. At lower latitudes, where the magnetic field lines are tilted, this approximation is more problematic and the use of this technique for magnetic field interpolation purposes during disturbed periods has been questioned (McLay & Beggan, 2010; Torta et al., 2017). However, other studies have shown very reasonable interpolation results in low latitude regions of South Africa (Bernhardi et al., 2008), Uruguay (Caraballo et al., 2013), and Brazil (Diogo, 2018). In particular, this last study was carried out in the central region of Brazil, adjacent to the area where the GICs are being estimated. SECS interpolation was exhaustively evaluated by Diogo (2018) by examining observed versus modeled magnetic field variations at different validation stations of a GDS survey, after ignoring the data corresponding to these validation points in the model input. It was observed that the method performance is greatly improved and very good estimates are obtained depending on the density of poles and the location of the grid area boundaries. Of note, SECS interpolation has only been used to generate potential geomagnetic fields at the Earth's surface and not to infer ionospheric electrical currents. Especially in low latitude regions there is no relationship between the SECS ionospheric equivalent current and the real ionospheric current (discussed in Vanhamäki and Juusola (2020)).

Following the results of Diogo (2018), a large density of poles and an extrapolation of the SECS equivalent current system to an area much larger than the region covered by the data were used to avoid the occurrence of artifacts and improve interpolation accuracy. Figure 4a displays the analysis area over which the elementary ionospheric current poles were placed. The altitude of the ionospheric equivalent current sheet was 100 km, and the distances of the poles in the grid (marked as brown dots) were 0.4° and 0.6° in the longitudinal and latitudinal directions, respectively. The intensities of the elementary currents during the magnetic storms were determined so that they provide the minimum error match with the EMBRACE magnetometer recordings. Next, the magnetic field was interpolated on the Earth's surface to the locations of the 63 GDS stations shown in Figure 1.

An essential role in the different stages of the GIC studies is played by the validation tests that aim to verify the capacity, precision, and limitations of the modeling. However, our limited data set and absence of GIC measurements prevent us from rigorously validating the interpolated geomagnetic fields (for a full validation exercise, see Pulkkinen et al. (2013)). Given these limitations, a more qualitative evaluation was chosen, verifying the physical reasonableness of the magnetic field inputs and outputs, as well as observing the robustness of the modeling in not generating interpolation artifacts in the calculated geomagnetic distortions. From the results shown in Figure 2, no significant variations are expected in the interpolated fields between nearby sites. Furthermore, due to its greater sensitivity to spikes and because it is commonly used as an indicator for the level of geomagnetically induced electric field on the Earth's surface (e.g., Viljanen et al., 2001), the time derivative of the magnetic field (dB/dt) was chosen to compare observation and model data.

Figure 4 exemplifies our validation of the interpolated dB/dt fields by showing a comparison of these fields predicted by the SECS model with the available observations. The northeast-southwest (NE-SW) profile highlighted in the central part of the PB was selected for comparison and will also be used in the next sections when discussing the calculated geoelectric field. The dB/dt values during the June storm are shown in Figures 4b and 4c, as measured at the three EMBRACE stations and derived by SECS at the selected profile sites. The results are in accordance with the assumptions previously established to consider adequate the interpolation of the magnetic field by SECS. No anomalous spikes are in the interpolated fields, and the dB/dt varies smoothly between the interpolated sites and the measured stations. In fact, the interpolation results across the profile resemble a latitudinal weighted average of observed data. It can be assumed that geomagnetic field variations during the studied magnetic storms are locally spatially homogeneous in this low-latitude region. Confirming this observation during other storms can be a central part of model transition to operations.

4.2. Synthetic Test of Geoelectric Field Calculation

To calculate the geoelectric fields, 345,535 points of the interpolated magnetic field time series were computed at each GDS survey site for the June storm (from 00:00:13 on 21 June to 23:59:07 UT on 24 June 2015) and 338,400 points for the December storm (from 23:59:44 on 18 December to 21:59:43 UT on 22 December 2015) with a sampling interval of 1 s. A window function was applied to the time series to minimize spectral leakage in the fast Fourier transform (FFT) calculation. The 1-D magnetic field spectra were calculated for the components B_x and B_y in the bandwidth 0.1–0.0001 Hz (periods of 10–10,000 s) at each site.

However, due to the limited period range of the MT and GDS data used to obtain the 3-D resistivity model, only periods above 300 s (frequencies below 0.0033 Hz) were considered for calculating the geoelectric field. The MT transfer functions (tensor impedances) of the 3-D resistivity model were derived at each GDS site over the same interval of 0.0001–0.0033 Hz, with 10 estimates per frequency decade equally spaced in a logarithmic scale, through forward calculation using the ModEM software package (Egbert & Kelbert, 2012; Kelbert et al., 2014).

In order to have the same frequency spectra in the magnetic field and in the MT model response, the real and imaginary parts of all impedance tensor components were interpolated to have a finer resolution in log-frequency space. A cubic spline interpolation method was chosen (Ahlberg et al., 1967) using 3*rd* degree polynomials between contiguous discrete points and ensuring that the first and second derivatives are continuous and smooth. The geoelectric field spectra were then computed by convolving the MT tensors with the magnetic fields as in Equation 3. The geoelectric field time series were finally derived by inverse FFT and removing the window effect.

To validate the developed computer code and perform a straightforward examination of the effects of Earth's resistivity structure on the geoelectric fields, synthetic geoelectric fields that would be induced by a geographically uniform reference geomagnetic signal were calculated. Similar exercises in other geoelectric field modeling studies used a sinusoidally varying geomagnetic field with a chosen set of oscillation frequencies and a defined amplitude (e.g., Bedrosian & Love, 2015; Divett et al., 2017; Wang et al., 2020). For this test, the time series of interpolated geomagnetic field changes at one location was used as the reference signal. In this case, the whole MT frequency band is considered simultaneously in evaluating the magnitude and direction of the induced geoelectric field. A peak recorded at 05:48 UT on 22 June in component B_x, related to the impact of the second CME on this storm, was chosen and its spectrum is defined here as $B_0(\omega)$. Three hypothetical scenarios were considered, with the magnetic field polarized in the directions south ($-B_x(\omega) = B_0(\omega)$, $B_y(\omega) = 0$), west ($B_x(\omega) = 0$, $-B_y(\omega) = B_0(\omega)$), and southwest $\left(-B_x(\omega) = -B_y(\omega) = \sqrt{2}B_0(\omega)\right)$.

Figures 5a–5c show maps during the chosen time instant with the spatial change in magnitude and direction of the derived two-dimensional (2-D) vector geoelectric field compared to magnetic variations ΔB and time

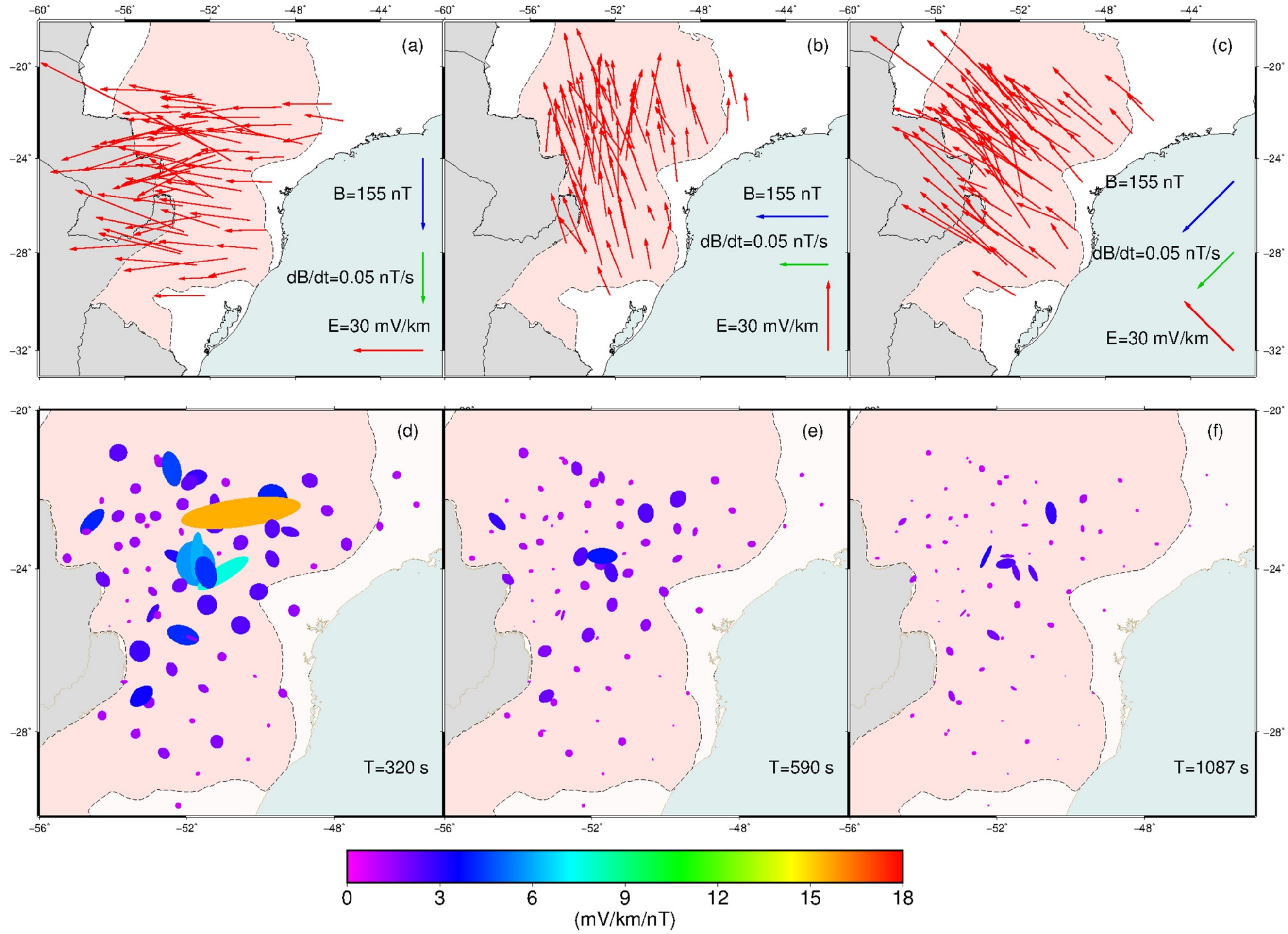

Figure 5. (a–c) Snapshots of the modeled geoelectric field (red arrows) for three different polarizations of the reference magnetic field B (blue arrows) and time derivative dB/dt (green arrows) at a peak recorded at 05:48 UT on 22 June 2015. The region covering the Paraná basin in Brazil is shown in pink. (a) Magnetic field polarized in the north-south direction, with reference arrows corresponding to 155 nT for B, 0.05 nT/s for dB/dt and 30 mV/km for E; (b) magnetic field polarized in the east-west direction; and (c) magnetic field polarized in the south-west direction. (d–f) Maps of surface E-polarized impedance amplitude $Z(D, f(xi, yi))/\mu$ for each geomagnetic deep sounding survey as a function of geoelectric field orientation for (d) $T = 320$, (e) $T = 590$, and (f) $T = 1{,}087$ s. The E-polarized impedance amplitude are expressed by the size and color of the ellipses.

derivative *dB*/*dt* for the three different polarizations of the magnetic field. A rough orthogonality between the magnetic and electrical vectors can be seen for the different polarizations. However, there are few sites where the geoelectric field vectors are really orthogonal to the direction of the polarized geomagnetic field and have almost the same magnitude, regardless of the direction of the inducing geomagnetic vector, as would be expected for a 1-D resistivity structure. In most cases, even in the thickest central part of the PB, geoelectric vectors have different magnitudes from one site to another and are oriented at acute and obtuse angles in relation to the inducing geomagnetic vector. These site-to-site differences are due to local differences in the impedance tensor, related to the Earth's 3-D resistivity structure.

The more substantial changes in vector direction and the largest amplitudes of synthetic geoelectric fields are observed in the central and northeastern portions of the PB, where the 3-D model shows high resistivities. On the other hand, the entire eastern part of the GDS array shows low amplitudes of the geoelectric field regardless of the polarization of the magnetic field. The expected coast line effect, in which geoelectric fields are amplified or attenuated in proximity to the prominent conductivity contrast between the continent and ocean (Love et al., 2018), is unobserved in this case. In a 2-D context, the geoelectric field would be amplified or damped depending on whether the inducing geomagnetic field (H) is parallel (H-polarization or transverse magnetic mode (TM)-mode) or normal (E-polarization or transverse electric mode (TE)-mode) to the coastline, respectively.

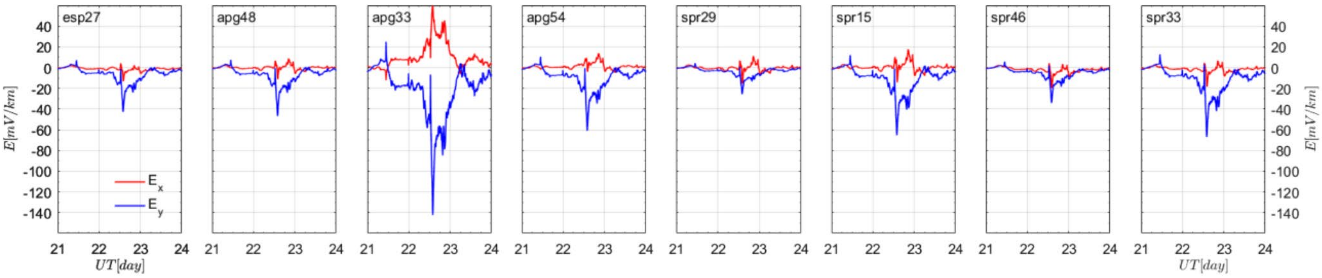

Figure 6. Geoelectric field E_x (red) and E_y (blue) time series for the storm of 21–24 June 2015 for each of the geomagnetic deep sounding locations of Figure 4, derived using the 3-D modeled impedance tensors from resistivity model in Figure 1c and low-pass filtered geomagnetic variations of Figures 2a and 2b.

The magnetic field polarized in the north-south (Figure 5a) and south-west (Figure 5c) directions correspond to the TM-mode in relation to different regions of the coast and are expected to lead to an amplification of the synthetic geoelectric vectors at sites approaching the coast. Unobservance of these amplification effects in the south-southeast region of Brazil is interpreted as due to the presence of high conductivity anomalies bordering the entire coastline (see Figure 1). Also, due to the shallow waters in this part of the South Atlantic Ocean (seafloor bathymetry less than 200 m up to 200 km from the coast), coast effects are relatively weak and do not extend over great distances onshore.

Using maps of E-polarized impedance (Berdichevsky & Dmitriev, 2008; Love et al., 2022; Murphy et al., 2021), the spatial variability of the surface impedance is illustrated in Figures 5d–5f. These maps show the impedance amplitude as a function of geoelectric field orientation at each GDS survey site for periods of 320, 590, and 1,087 s, considering a synthetic unit-inducing geomagnetic field (1 nT). Following the procedure described by (Murphy et al., 2021), the radial scale is given in (mV/km)/(nT), whereas the polar axis is defined in geographic azimuth. For a specific MT impedance tensor at a specific period, the length of the ellipse's major axis shows the size of this maximum geoelectric field and points in the direction of the largest achievable geoelectric field. These geoelectric fields exhibit substantial differences in amplitude and polarization at each particular period. In the eastern part of the PB, a one-dimensional depth-dependent distribution of solid-Earth electrical conductivity is illustrated by circles in the polarized impedance polar diagram. The central and northeastern portions of the PB, which have strong resistivities according to the 3-D model (see Figure 1c), are distinguished by the largest ellipses in the resulting E-polarized impedance diagrams, which reflect lateral conductivity contrast. In this location, where impedances are strongly polarized and typically of large amplitude, for a 1 nT source magnetic field, the highest achievable geoelectric field among the GDS sites is 18 (mV/km)/(nT), and is directed approximately east-west. For each period represented in Figures 5d–5f, the maximum-to-minimum ratio of the amplitudes of these tensors is 127.2, 65.7, and 147.5, respectively.

4.3. Geoelectric Time Series During the Magnetic Storms

The same procedure used in the synthetic test was applied to derive the geoelectric fields from the interpolated geomagnetic variations during the two magnetic storms. This approach is similar to that described by Love et al. (2022), who investigated relationships pertinent to GICs reported on electric-power systems across the contiguous United States during the 13–14 March 1989 magnetic storm. Figure 6 presents the geoelectric field time series estimated in the north-south (E_x) and east-west (E_y) directions during the June storm at the eight chosen sites of Figure 4. Figure 6 is instructive in showing the effects of magnetic field polarization and resistivity distribution on the calculated geoelectric field. Stronger geomagnetic variations are usually observed in the S-N direction (B_x), close to the Earth's magnetic meridian, and cause the geoelectric field to have a much larger magnitude in the east-west (E-W) direction (E_y) than in the south-north (S-N) direction (E_x). Also, considering the same polarization for the magnetic field, the greatest magnitudes of the geoelectric field are observed in more resistive regions. This can be seen, for example, when comparing the magnitude of the geoelectric field E_y modeled for station apg33 with its neighboring stations apg48 and apg54. The peak magnitudes of the E_y field for these three sites observed around 20:01 UT on 22 June was −46.7 (apg48), −142.2 (apg33), and −61.0 mV/km (apg54).

Magnetic storms are transient phenomena that disturb currents in both the magnetosphere and the ionosphere and are the main causes of high rates of change in horizontal geomagnetic components observed on the Earth's surface. These stormy disturbances often vary over a wide range of frequencies and as a consequence give rise to geoelectric fields with very different spectral content. Geoelectric fields with different frequencies of oscillation

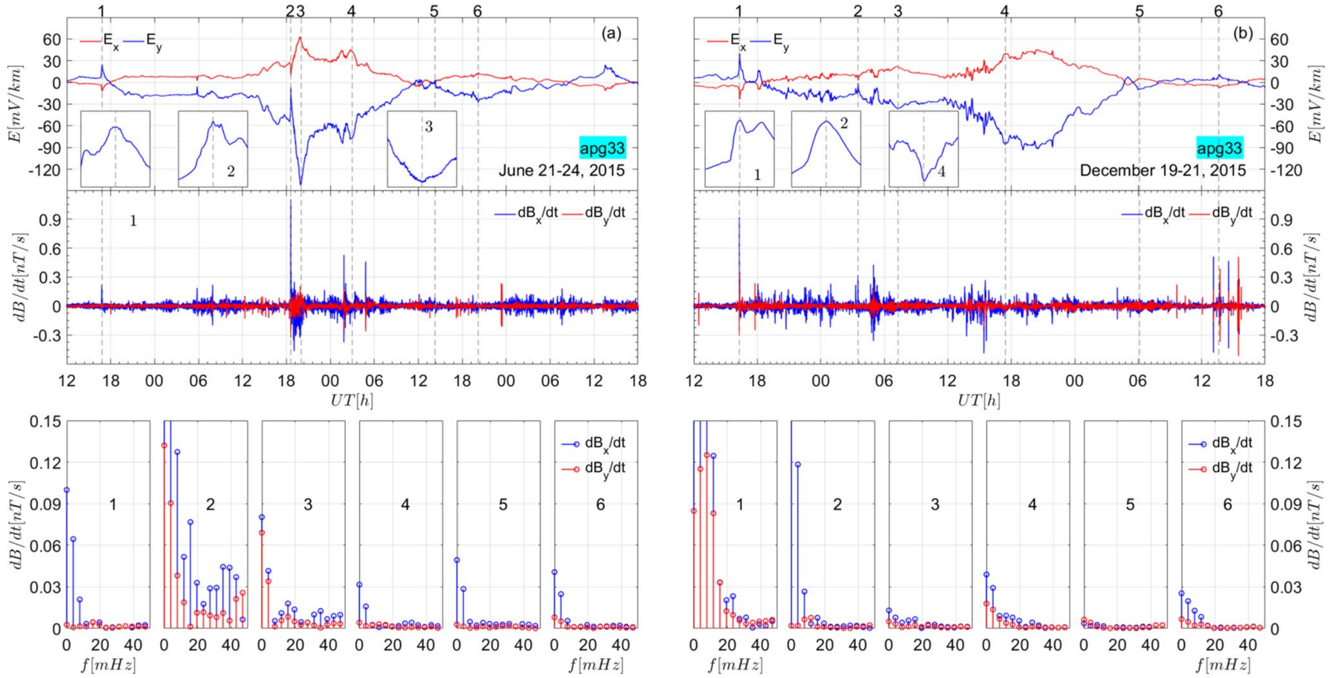

Figure 7. Comparison of calculated geoelectric field, and instantaneous *dB*/*dt* power spectra at site apg33. The upper graphs show estimated geoelectric field time series (E_x and E_y) during the two magnetic storms. Intermediate graphs show the corresponding dB_x/dt and dB_y/dt during that time period. Insets in the upper panels show zoomed plots around 200 s (snapshots 1 and 2 of the June storm, 1, 2, and 4 of the December storm) and 900 s (snapshot 3 of the June storm) of time instants of the E_y component for the two storms (maximum magnitude in June, 1–25.1, 2–6.7, and 3–−142.2 mV/km, maximum magnitude in December, 1–40.36, 2–−1.2, and 4–−86.6 mV/km). At the bottom are snapshots of dB_x/dt and dB_y/dt power spectra at the time instants identified by vertical dashed lines in the graphs above.

can also affect technological systems on the surface differently. Thus, an important aspect in GIC studies is to correlate the main peaks of geoelectric field variation with the characteristics of the rate of change of the magnetic field.

A comparison of the estimated geoelectric field time series during the two storms at apg33 with the time derivative of the magnetic field (*dB*/*dt*) and its Fourier spectral power at selected instants is shown in Figure 7. The upper and intermediate panels identify instants in the geoelectric field time series and in the magnetic field time derivatives (six vertical dashed lines in each storm) that correspond to some chosen peaks in the geoelectric field. These time instants are presented in Table 2 and include the storm sudden commencement (SSC), the third CME impact and the maximum geoelectric field of the June storm (snapshots 1, 2, and 3, respectively), and the SSC of the December storm (snapshot 1). At the bottom of Figure 7 are snapshots of *dB*/*dt* spectrograms around (120 s) each of the time instants. Parseval's relation (Smith, 2013) was used to indicate how the signal energy is distributed over frequencies. A Hann window function was utilized to resolve a weak frequency while dealing with possible strong intrudes at the same time due to its wide dynamic range.

Table 2
Time Instants of the Selected Snapshots Presented in Figure 7

June 2015			December 2015		
Snapshot	Date	Time (UT)	Snapshot	Date	Time (UT)
1	21 June	16:49:50	1	19 December	16:18:32
2	22 June	18:35:14	2	20 December	03:31:29
3	22 June	20:01:04	3	20 December	07:18:08
4	23 June	02:58:10	4	20 December	17:26:37
5	23 June	14:16:43	5	21 December	06:07:53
6	23 June	20:10:59	6	21 December	13:36:42

The spectral power during geomagnetic disturbances is expected to be distributed over a wide range of frequencies, contrary to what is observed in the spectral content of all selected peaks with a significant predominance of dB_x/dt amplitudes and of low-frequency components (generally less than 10 mHz). The only exception is the peak amplitude dB_x/dt in the June storm, identified as snapshot 2 in that storm (third CME impact). It presents the highest spectral power at low frequencies but also has important high-frequency spectral components. For the December storm, the highest *dB*/*dt* and spectral power are observed at peak 1 (SSC). Low energy at higher frequencies is typical of low latitude regions and is related to the correlation between geomagnetic latitude and increased *dB*/*dt* levels (Pulkkinen et al., 2012). On the other hand, longer-period disturbances with larger amplitudes can be effective drivers of sustained and large geoelectric fields and GICs.

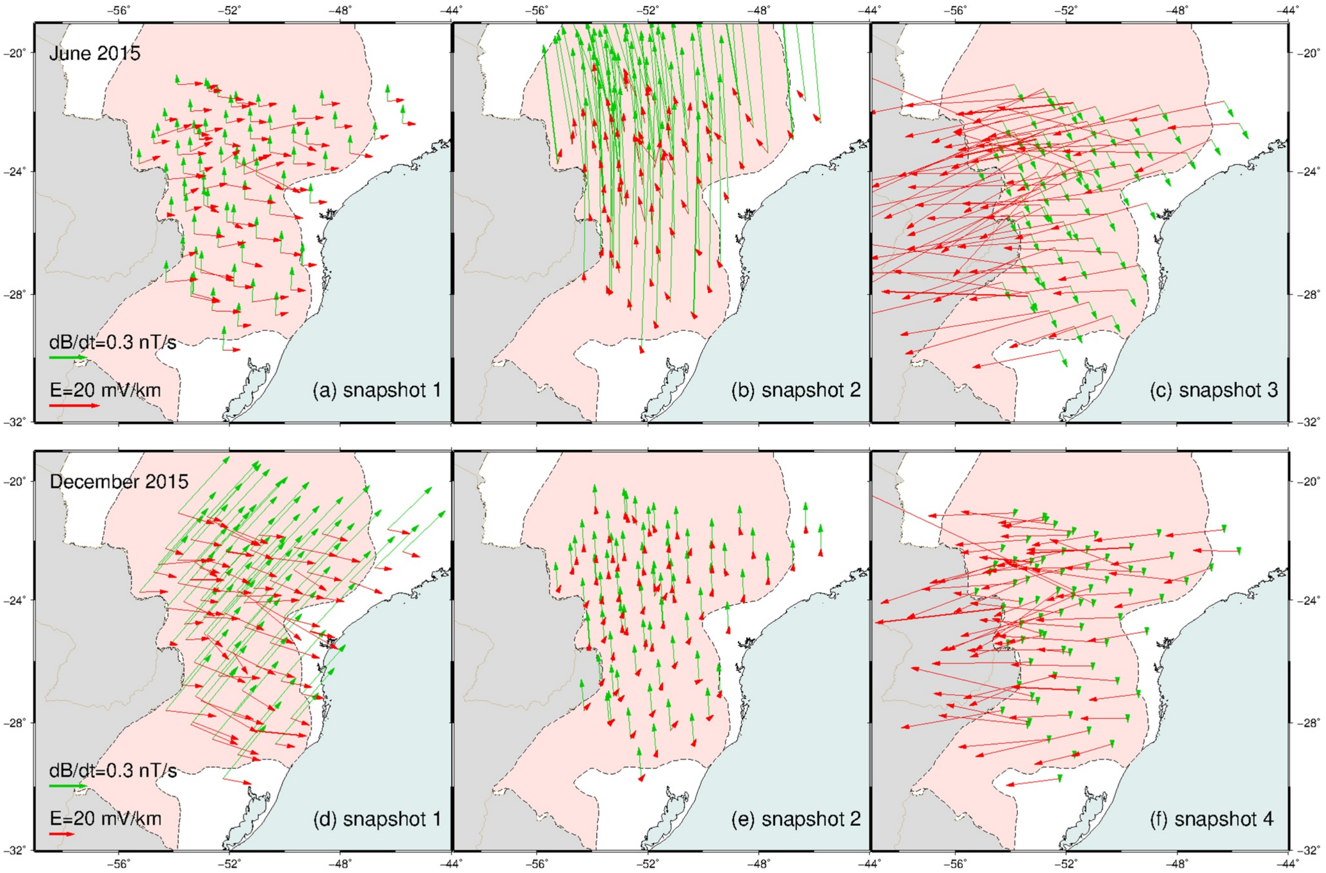

Figure 8. Selected snapshots of the modeled geoelectric field (red arrows) and interpolated *dB*/*dt* (green arrows) during the two storms. Time instants for the June storm (upper panels) and the December storm (lower panels) can be identified by the snapshot number in Table 2.

Not only the magnitude of the geoelectric field is important for GIC modeling, but the orientation of the vector relative to a power network also plays a critical role (Dimmock et al., 2020; Viljanen & Pirjola, 2017). Because of this, different patterns of field vectors in a given area with the same regional mean can produce very different GICs. An accurate determination of the spatial structure of the geomagnetic variations and inferred geoelectric fields must then be taken into account with the scale of the network, which is usually done in the form of snapshots of both parameters during the most intense events.

Figure 8 shows the vector form of the resulting geoelectric fields at all GDS sites during three representative snapshots of each storm. Snapshots of the interpolated *dB*/*dt* for all sites at the same time instants are also shown for comparison. As expected from the larger dB_x/dt magnitudes shown in Figure 7, the *dB*/*dt* vector direction is preferably oriented in the north-south (N-S) direction. The main exception is in the SSC of the December storm (Figure 8d) where a north-east (N-E) direction is observed. On the other hand, the direction and magnitude of the geoelectric field vector vary greatly for different time instants of the magnetic storms, not necessarily following the instantaneous direction and magnitude of the *dB*/*dt* vector. In fact, the rough orthogonality between the geoelectric field vector and the *dB*/*dt* vector observed in the synthetic test in Figures 5a–5c is not observed in the real situation during the two storms. Likewise, the magnitudes of the *dB*/*dt* vectors do not necessarily correspond to the magnitudes of the geoelectric field at the same time instants. This can be seen by comparing snapshots 2 and 3 of the June storm. The large N-S oriented *dB*/*dt* of snapshot 2 has an associated geoelectric field vector of small magnitude approximately parallel to this same direction. In contrast, the smallest magnitude *dB*/*dt* of snapshot 3 is associated with a very large magnitude geoelectric field vector in the orthogonal direction.

These apparent discrepancies can be explained by the fact that the instantaneous geoelectric field is not only a function of the instantaneous *dB*/*dt*, but also embeds information from the preceding magnetic field. This can be shown analytically, for a simplified, fully homogeneous Earth, by equations relating the S-N (E_x) and E-W

(E_y) components of the geoelectric field to the time derivative of the E-W (B_y) and S-N (B_x) geomagnetic field components, respectively (Pirjola, 2002)

$$E_x(t) = \frac{1}{\pi\mu_0\sigma}\int_{-\infty}^{t}\frac{1}{\sqrt{t-u}}\frac{dB_y(u)}{dt}\,du \tag{8}$$

$$E_y(t) = -\frac{1}{\pi\mu_0\sigma}\int_{-\infty}^{t}\frac{1}{\sqrt{t-u}}\frac{dB_x(u)}{dt}\,du \tag{9}$$

where σ represents a uniform conductivity of the Earth at the studied location. These equations indicate that the electric field depends not only on the time derivative of the geomagnetic field (shown inside the integral), but also on the previous values of the magnetic field. The weighting of the previous values of the magnetic field decreases with time by the $\sqrt{t-u}$ factor in the denominator. For a fully 3-D Earth, this can be explained by decomposing the complex impedance into a real apparent resistivity (magnitude) and a phase, where the phase describes the time lag (or lead) of the electric field relative to the magnetic field.

For snapshot 2 of the June storm, it can be seen in Figure 7 that the geoelectric field E_y just before the dB_x/dt peak was oscillating around −50 mV/km due to the two previous CME impacts. The large positive spike in dB_x/dt from the arrival of the third CME (secondary SSC) causes this geoelectric field to shift to approximately −5 mV/km. For the E_x geoelectric field, the effect of the negative dB_y/dt peak was to reduce the geoelectric field from 25 to 10 mV/km. Due to the inverted polarization of the dB/dt large spike in relation to the preceding values of the geoelectric field, the magnitude of the instantaneous geoelectric field vector resulting in this snapshot is low (Figure 8). This modeling result is at variance with the proposition that SSC events could produce large geoelectric fields, and consequently associated GICs, at low geomagnetic latitudes (Kappenman, 2003). None of the three recorded SSCs (snapshots 1 and 2 of the June storm and snapshot 1 of the December storm) were capable of producing large geoelectric fields during these events.

On the other hand, Figure 7 also shows that the negative spike in dB_x/dt from snapshot 3 of the June storm follows a sequence of several negative spikes in dB_x/dt during the magnetic storm main phase. This causes an excursion of the geoelectric field E_y to values below −120 mV/km before that time instant (long-period variation). The large negative magnitude of the geoelectric field E_y in snapshot 3 is therefore related to the cumulative effects of all these several dB_x/dt with the same negative polarity, which result in a long-period ondulation. Similarly, the geoelectric field E_x is enhanced in the same snapshot by an earlier positive dB_y/dt sequence. The result is the large magnitude observed in the instantaneous geoelectric field vector seen in Figure 8, even though the dB/dt vector magnitude is not substantial at that time instant.

Due to the close link between the time derivative of the geomagnetic field and the level of the induced geoelectric field, dB/dt has been proposed as a reasonable proxy for GIC activity (Viljanen et al., 2001). However, some examples are found in the literature indicating the inadequacy of the dB/dt metric to characterize GIC. Trichtchenko and Boteler (2006) and Watari et al. (2009) present examples from Canada and Japan, respectively, where the observed GIC tends to follow the variation of the local geomagnetic field rather than its time derivative. These results were explained by the presence of local geological anomalies that can create sharp gradients in conductivity. The June 2015 storm discussed here represents another case study where the dB/dt metric fails, in this case associated with the relationship of the geoelectric field to previous values of the magnetic field. In fact, the unusual creation of multiple CMEs connected with M-class flares that triggered this storm had a large effect on this relationship between instantaneous dB/dt and geoelectric field vectors. A similar result on the inadequacy of dB/dt as a proxy for GIC activity during this storm was obtained by Heyns et al. (2021) when analyzing long-period pulsations. It should also be considered that the linear relationship between the local dB/dt and the local geoelectric field, or the power-line average of the ground-level geoelectric field (which determines the GICs), breaks down in the presence of substantial spatial heterogeneity in the Earth's electrical conductivity. A general discussion of the effects of 3-D variations in Earth's resistivity on the ground geoelectric field, and the GICs, and a summary of relevant studies can be found in Kelbert (2020).

5. Calculating GIC

Following the nodal network approach of the LP method, the calculation of GIC in transmission lines requires the values of the geoelectric fields in each cell of the ground resistivity model where the substations are located and also in those through which the transmission lines pass. Although the geoelectric field can be computed for each horizontal cell of the 3-D model (10 × 10 km scale), our choice was to use the derived values in the observed data cells (∼100 × 100 km scale). Delauney triangulation is often used in GIC studies (e.g., Bonner & Schultz, 2017; Lucas et al., 2018) and produces smoother interpolated fields between measurement sites. However, in regions with a small number of sites, such as at the edges of our transmission lines, extrapolated geoelectric fields can be unrealistic. As a first approximation, the nearest neighbor method that produced reliable interpolation results between cells containing measurement sites and extrapolated fields with apparently less significance errors was chosen.

Accurate values of the power network elements for GIC calculations are not available and therefore estimates of substation grounding and transformer winding resistances had to be made. According to the bidding terms and prescribed technical requirements for transmission line installations in Brazil, the resistance per unit of length must range from 0.0174 to 0.028 Ω/km for a 525 kV power grid (ANEEL, 2016). As we mainly look for the most exposed regions in the network, the minimum value (0.0174 Ω/km) was used to obtain the maximum GIC magnitudes. Furthermore, according to the ANSI/IEEE80 norm (IEEE, 2007) that electricity companies in Brazil must follow the maximum recommended grounding resistance is 1 Ω. Based on the best fit between calculated and measured GICs in the neutral of a power transformer of a substation in central Brazil during a geomagnetic storm on 8 October 2013 (Espinosa et al., 2019) and parameters suggested by Barbosa, Hartmann, and Pinheiro (2015), a ballpark value of 0.43 Ω was assumed for all grounding resistances in the hypothetical 525 kV power transmission network.

The instantaneous GIC magnitudes calculated by the LP method on the network nodes during the snapshots in Table 2 are represented by green circles in Figure 9. The vector form of the geoelectric field centered on the corresponding GDS site location is also shown (same as Figure 8), with those used to calculate GICs via the nearest neighbor technique highlighted. The maximum magnitudes of the modeled GICs are observed in snapshots that are representative of the main phase of both storms (snapshot 3 for June and 4 for December). Two substations stand out as those with the highest GIC magnitude. One corresponds to node 2 in the northern part of the network, which is located in the region where the greatest geoelectric field magnitude is observed, and its vector direction is approximately parallel to the transmission line direction. The other corresponds to node 12 located in the central part of the PB, a substation connecting several mainly E-W branches of the grid and also a region with a strong geoelectric field. Modeled GIC magnitudes were 9.08 (node 2) and 7.69 A (node 12) for the June storm and 4.75 (node 2) and 5.03 A (node 12) for the December storm. The minimum magnitudes were modeled for substation 6, located on the high conductivity anomaly along the basin axis, and substations 16–20 and 22–23, located on the strong conductors bordering the continental margin. The maximum GIC magnitudes for these substations were observed in the June storm, but were less than 2.5 A.

Figure 10 shows time series of GIC magnitudes calculated for each substation in the hypothetical power grid during the June storm, the strongest of the two storms analyzed. Two effects are highlighted in this figure: substations with opposite GIC polarity and substations with large GIC. Substations with opposite GIC polarity to the remaining substations are concentrated along a northeast-southwest branch on the northern edge of the power grid (substations 1–5). The inverted GIC polarity is likely associated with the edge effect whereby the GIC typically flows to/from the ground through substations at the edge of the network (Boteler & Pirjola, 2017).

On the other hand, it would be expected that geometric properties of the grid (edge effect) would cause large GICs to occur at the corners of the grid and this is observed in many studies worldwide (e.g., Torta et al., 2014; Zheng et al., 2014). However, Figures 9 and 10 show that the substations experiencing large GICs are found in the central part of the network, where the transmission lines are oriented mainly east-west and a higher concentration of substations is observed, and in the localized region of high resistivity under substation 2 of the northern branch. The possibility of larger GICs concentrated in the inner parts of the grid rather than its edges was pointed out in simulation studies for the Japanese network (Nakamura et al., 2018). They indicated that the topology of the network, its relationship to the direction of the geoelectric field, and localized effects of ground resistivity can generate larger GICs in different parts of the network.

The substations with the highest GIC in Figure 10 can then be related to various effects, including the predominantly E-W direction of the geoelectric field with higher magnitude, the concordant E-W direction of transmission lines in the central part of the grid, and lower subsurface conductance values in the same region beneath the PB. Furthermore, as discussed earlier, the 3-D model shows strong crustal high conductivity anomalies along the

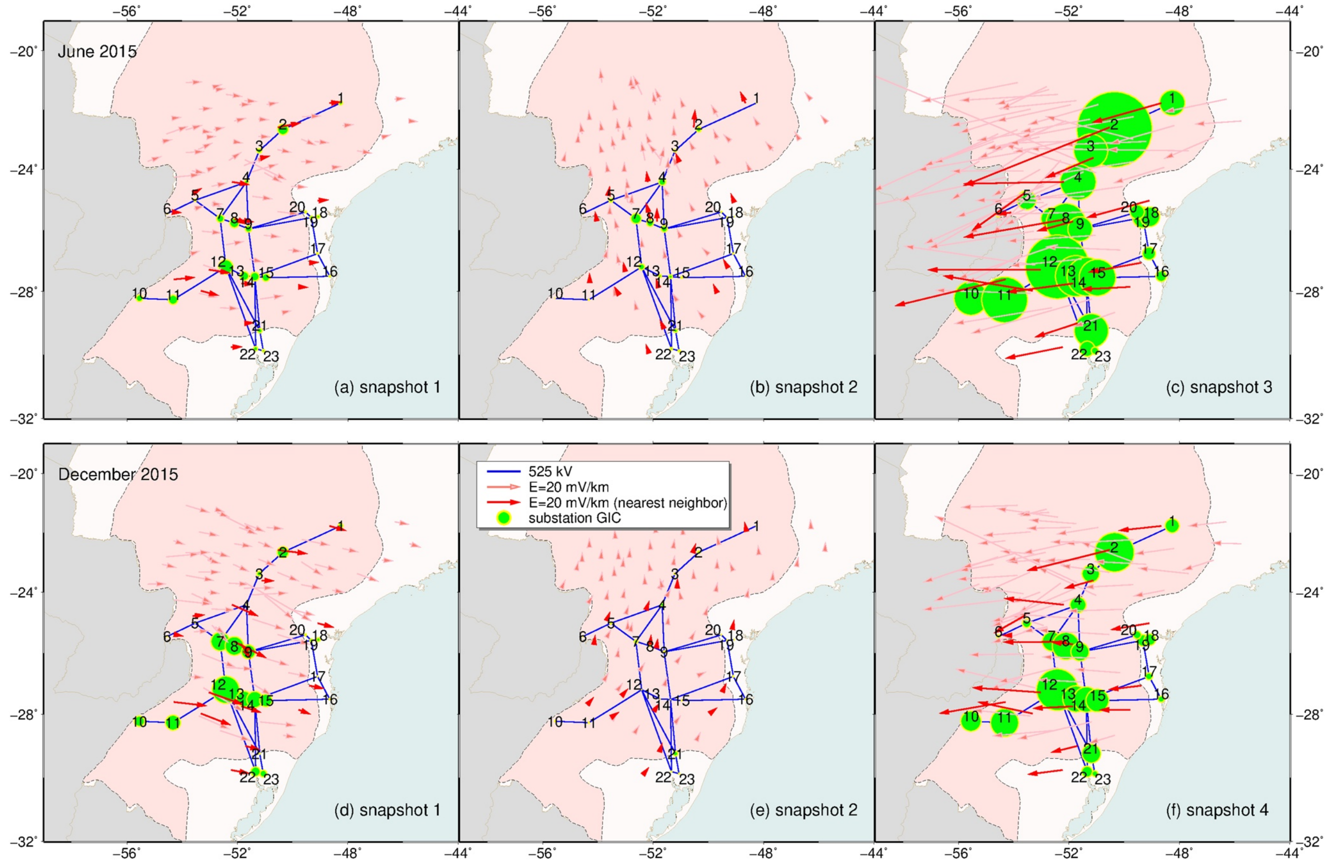

Figure 9. Geoelectric field and Geomagnetically induced current (GIC) calculated during the selected snapshots for the June and December 2015 storms. Red arrows show the instantaneous vector geoelectric field, with those chosen for the GIC calculation highlighted. Green circles are the instantaneous GIC modeled on the 525 kV transmission line substations (in blue). GIC magnitude is proportional to the diameter of the circles, with the highest value at substation 2 for snapshot 3 of the June storm corresponding to 9.08 A.

coastline, which contribute to dampening GIC estimates in this area. More importantly, this figure indicates possible substations where installation of GIC sensors would be beneficial to validate the modeling methodology.

6. Discussion

The quantitative GIC values derived for the June and December 2015 magnetic storms are rough estimates because of the inherent assumptions made in the modeling approach. Accurate and detailed computation of GIC time series in our power grid network is not the main goal of this study. A guide to the relative importance of system parameters when estimating GIC impacts on a power grid is provided by Zheng et al. (2014). In our case, in addition to the imprecise information about the network parameters and omission of transmission lines of lower voltage elements, the limitation of the 3-D model used to calculate the geoelectric field also warrants consideration.

Although the geomagnetic field has a resolution of 10 s and the impedance tensor elements derived by forward calculation could have the same resolution, the modeled geoelectric field presents a lower resolution. This is because the 3-D resistivity model was mainly based on GDS data acquired with a sampling of 60 s (Nyquist limit of 120 s), so that only periods greater than 300 s (frequencies less than 0.0033 Hz) were considered in the geoelectric field calculation. At depths shallower than a critical depth determined by the subsurface resistivity structure and the highest frequency data available, there is essentially no structural resolving power and electromagnetic induction methods become insensitive to structural details while remaining sensitive to the bulk conductance (vertically integrated conductivity) of these surface layers. Thus, the resolution of the near-surface part of the model is very low, especially outside the sedimentary basin where resistive structures are observed on the surface. In this case, the modeled geoelectric values should be considered lower estimates of potential

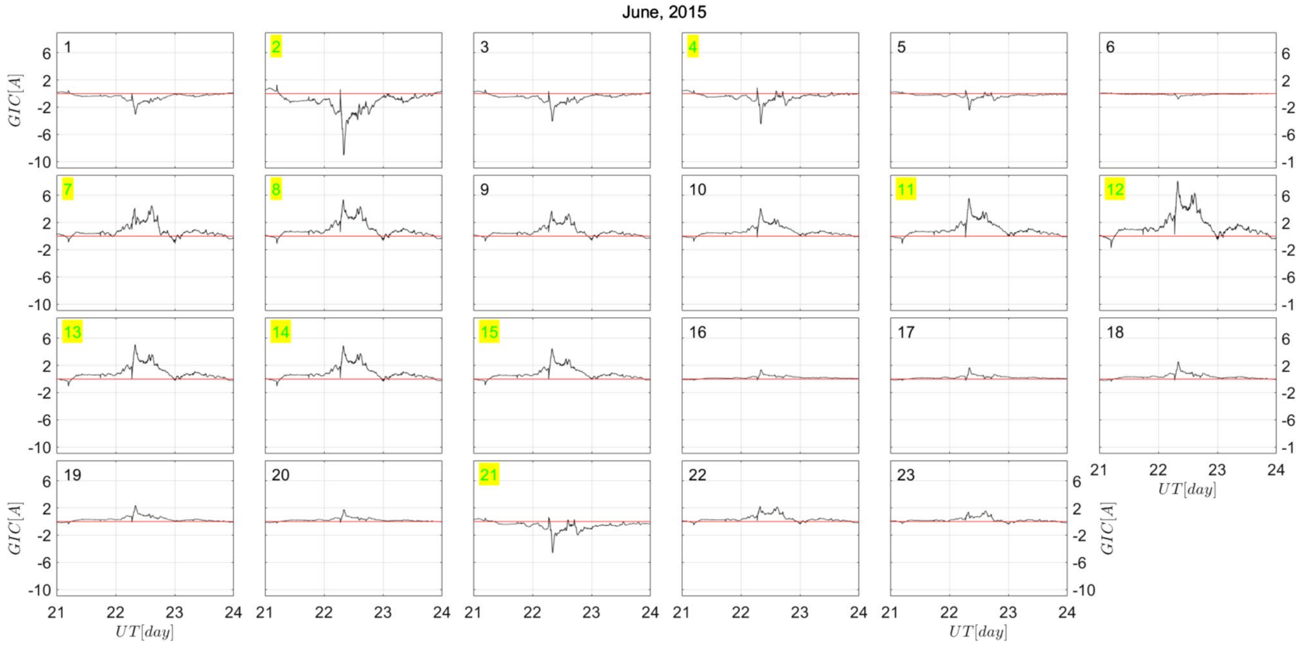

Figure 10. Time series of the resulting Geomagnetically induced current (GIC) modeling at the 23 substations of the hypothetical 525 kV transmission line during the June storm. Substations with GIC magnitudes greater than 4.5 A are highlighted in yellow and indicate possible nodes for future installation of GIC sensors.

real values. However, within the basin, MT surveys (e.g., Maurya et al., 2018; Padilha et al., 2015) show that the volcanic-sedimentary package is quite homogeneous in terms of electrical resistivity, approaching a 1-D situation. Variations in the geoelectric field occur mainly in the crystalline basement under the basin and are correctly represented in the model.

Apart from the aforementioned limitations for calculating the geoelectric field, the method chosen to interpolate this field for GIC modeling also presents serious issues. The interpolation technique using the irregular 100 km grid of observed data cells forces the geoelectric field to be homogeneous between some substations. This procedure eliminates local galvanic distortions associated with fine-scale heterogeneities in the near-surface conductivity structure but causes lateral variations in conductance to be very approximate. The use of local transfer functions or regional spatial averaging to represent conductivity for geoelectric field modeling is widely discussed in the literature (e.g., Bedrosian & Love, 2015; Bonner & Schultz, 2017; Kelbert et al., 2019). Alternative methods not requiring a realistic geoelectric field and its integration over power lines for GIC calculation can be further considered (e.g., Kelbert & Lucas, 2020). Validation efforts of modeled GICs can help answer these questions.

Modeling results are based only on two magnetic storms, the largest recorded since starting the operation of the EMBRACE magnetometer network. It is well known that magnetic storms vary substantially between different occurrences, such that any storm is essentially unique (e.g., Kamide & Maltsev, 2007). A small change in the ionospheric source during a geomagnetic field disturbance can potentially produce large changes in both the magnitude and orientation of the resulting geoelectric fields on the Earth's surface. From a risk assessment perspective, what matters is the availability of a data set including a substantial number of severe space weather events. This is because substations experiencing large GIC in a network are not necessarily the same during different magnetic storms (e.g., Blake et al., 2016). More statistics would be beneficial to reliably assess hot spots and potential GIC hazards in this power transmission system, considering large time scales.

Figures 2 and 3 show that the geomagnetic field can be assumed spatially homogeneous during the two magnetic storms. This is not unexpected for low magnetic latitudes but also needs to be confirmed with a larger number of events. Field homogeneity can be used to increase computational speed for operational GIC hazard assessment. A sophisticated and computationally demanding technique such as SECS may not be necessary for magnetic field interpolation purposes in this region during magnetically disturbed periods. Simpler techniques, such as the nearest neighbor used here for GIC modeling or latitudinal weighted average using distant EMBRACE magnetometers, may be adequate enough for magnetic field interpolations.

The simulation results from this study can be used to determine both GIC mitigation strategies for the power transmission system of southern Brazil and relevant locations for installing monitoring equipment. Mitigation efforts can be initially focused on the identified cluster of hot spots at substation 2, located on the northern edge of the study area, and in the central parts of the modeled grid, where small conductance and E-W lines can generate large geoelectric fields and GIC. Sensors can then be installed in some of these substations, avoiding those with multiple connections. The main candidates are highlighted in Figure 10, with emphasis on nodes 2, 8, 11, 13, or 15. An extreme end-member of lower current could also be chosen for validation processes and the NE-SW line at the northern edge may be the obvious choice. Avoiding corner points and endpoints of this line, node 3 may be the best option. However, the final choice would need to be made together with the transmission line operators according to the characteristics and limitations of the different substations.

7. Summary and Potential Future Work

The current state-of-the-art in GIC calculation was implemented to simulate currents produced during two intense geomagnetic storms in a hypothetical representation of a power network in southern Brazil. Available 3-D electrical resistivity model and low-pass filtered signal of 1-s geomagnetic variations were used to obtain geoelectric fields during storms. The difference between the transfer functions above 300 s and the low-pass filtered geomagnetic data above 10 s lessens the temporal resolution of the estimated geoelectric field. Simulation results indicate possible threats in an isolated substation near the northern edge of the grid and in a cluster of hot spots in the central part of the grid, where small conductance is observed and the relative orientation of the instantaneous geoelectric field coincides with E-W transmission lines. Due to the various assumptions made in the modeling approach, an accurate GIC calculation is not possible. The study focuses primarily on prospecting substations with potential GIC hazards and where to install future monitoring equipment for validation efforts.

Future work is planned to concentrate on operational space weather activities targeting regional forecasts. The next step could be to use the results of this stage to plan the installation of GIC sensors in the chosen substations. Further information also would be beneficial to improve GIC calculations. As discussed earlier, the electrical resistivity structure was mainly obtained by fitting long-period GDS data. Impedance tensors for geoelectric field modeling were derived from the 3-D resistivity model. This model can be updated to enhance upper crustal resolution with ongoing MT surveys in the PB. It would be necessary to include low voltage transmission lines in the power grid model and use realistic information about transformer resistances and substation grounding. This means intensifying end-user participation in the modeling and validation processes would be beneficial. Finally, the methodology developed for this region could be expanded to other regions of Brazil where similar GDS arrays (see Bologna et al. (2014), for distribution of GDS stations in Brazil) and MT soundings generally concentrated along profiles are available. In the absence of detailed continental-scale MT grids, such as the Australian Lithospheric Architecture Magnetotelluric Project, which has stations spaced about 50 km apart and collects MT data across the entire Australian continent, the USArray and USMTArray programs, which have collected MT surveys in the United States since 2006 and with stations spaced about 70 km, and China's Deep Exploration Technology and Experimentation (SinoProbe) project, which produced MT arrays across the country with a grid resolution of $4° \times 4°$ and $1° \times 1°$, this is what we propose at this point.

Data Availability Statement

The 2015 geomagnetic storm data are available with the EMBRACE program (http://www2.inpe.br/climaespacial/portal/en/), and Dst index is from the WDC Kyoto (http://wdc.kugi.kyoto-u.ac.jp/). MT and GDS data sets are available in the open data repository Zenodo (https://doi.org/10.5281/zenodo.7186637). The 3-D resistivity model in its digital format is available from the IRIS EMC repository (http://ds.iris.edu/ds/products/emc/).

Acknowledgments

The study was supported by CNPq Grants (306390/2017-5, 301476/2018-7, 141376/2019-8, and 313536/2022-8). We thank the Brazilian Ministry of Science, Technology and Innovation and the Brazilian Space Agency for their support of this research. We also thank Dr. Jeffrey Love and two anonymous reviewers for their helpful comments and suggestions on this work. Any use of trade, firm, or product names is for descriptive purposes only and does not imply endorsement by the U.S. Government.

References

Abdu, M. A., Batista, I. S., Carrasco, A. J., & Brum, C. G. M. (2005). South Atlantic magnetic anomaly ionization: A review and a new focus on electrodynamic effects in the equatorial ionosphere. *Journal of Atmospheric and Solar-Terrestrial Physics*, *67*(17–18), 1643–1657. https://doi.org/10.1016/j.jastp.2005.01.014

Ahlberg, J. H., Nilson, E. N., & Walsh, J. L. (1967). *The theory of splines and their applications*. Academic Press.

Alken, P., Thébault, E., Beggan, C. D., Amit, H., Aubert, J., Baerenzung, J., et al. (2021). International geomagnetic reference field: The thirteenth generation. *Earth Planets and Space*, *73*(1), 49. https://doi.org/10.1186/s40623-020-01288-x

Almeida, F. F. M., Brito Neves, B. B., & Carneiro, C. D. R. (2000). The origin and evolution of the South American Platform. *Earth-Science Reviews*, *50*(1), 77–111. https://doi.org/10.1016/S0012-8252(99)00072-0

Amm, O. (1997). Ionospheric elementary current systems in spherical coordinates and their application. *Journal of Geomagnetism and Geoelectricity*, *49*(7), 947–955. https://doi.org/10.5636/jgg.49.947

Amm, O., & Viljanen, A. (1999). Ionospheric disturbance magnetic field continuation from the ground to the ionosphere using spherical elementary current systems. *Earth Planets and Space*, *51*(6), 431–440. https://doi.org/10.1186/BF03352247

ANEEL. (2016). *Leilões de Transmissão. Características e Requisitos Técnicos Básicos das Instalações de Transmissão*. Agência Nacional de Energia Elétrica. Retrieved from https://antigo.aneel.gov.br/transmissao4

Astafyeva, E., Zakharenkova, I., & Alken, P. (2016). Prompt penetration electric fields and the extreme topside ionospheric response to the June 22–23, 2015 geomagnetic storm as seen by the Swarm constellation. *Earth Planets and Space*, *68*(1), 152. https://doi.org/10.1186/s40623-016-0526-x

Barbosa, C., Alves, L., Caraballo, R., Hartmann, G. A., Papa, A. R. R., & Pirjola, R. J. (2015). Analysis of geomagnetically induced currents at a low-latitude region over the solar cycles 23 and 24: Comparison between measurements and calculations. *Journal of Space Weather and Space Climate*, *5*, A35. https://doi.org/10.1051/swsc/2015036

Barbosa, C., Hartmann, G., & Pinheiro, K. (2015b). Numerical modeling of geomagnetically induced currents in a Brazilian transmission line. *Advances in Space Research*, *55*(4), 1168–1179. https://doi.org/10.1016/j.asr.2014.11.008

Bedrosian, P. A., & Love, J. J. (2015). Mapping geoelectric fields during magnetic storms: Synthetic analysis of empirical United States impedances. *Geophysical Research Letters*, *42*(23), 10160–10170. https://doi.org/10.1002/2015GL066636

Berdichevsky, M. N., & Dmitriev, V. I. (2008). The Magnetotelluric Response Functions. In M. N. Berdichevsky & V. I. Dmitriev (Eds.) *Models and Methods of Magnetotellurics* (pp. 1–49). Berlin, Heidelberg: Springer. https://doi.org/10.1007/978-3-540-77814-1_1

Bernhardi, E. H., Cilliers, P. J., & Gaunt, C. T. (2008). Improvement in the modelling of geomagnetically induced currents in southern Africa. *South African Journal of Science*, *104*(7–8), 265–272. https://doi.org/10.10520/EJC96821

Bizzi, L. A., Schobbenhaus, C., Gonçalves, J. H., Baars, F. J., Delgado, I. M., Abram, M. B., et al. (2001). *Geologia, Tectônica e Recursos Minerais do Brasil: Sistema de Informações Geográficas–SIG e Mapas na Escala 1: 2 500 000. 4a Edição, 4 CD-rom*. Companhia de Pesquisa e Recursos Minerais-CPRM.

Blake, S. P., Gallagher, P. T., Campanya, J., Hogg, C., Beggan, C. D., Thomson, A. W. P., et al. (2018). A detailed model of the Irish high voltage power network for simulating GICs. *Space Weather*, *16*(11), 1770–1783. https://doi.org/10.1029/2018SW001926

Blake, S. P., Gallagher, P. T., McCauley, J., Jones, A. G., Hogg, C., Campanya, J., et al. (2016). Geomagnetically induced currents in the Irish power network during geomagnetic storms. *Space Weather*, *14*(12), 1136–1154. https://doi.org/10.1002/2016SW001534

Bologna, M. S., Padilha, A. L., Pádua, M. B., Vitorello, I., & Chamalaun, F. H. (2014). Paraguay-araguaia belt conductivity anomaly: A fundamental tectonic boundary in South American platform imaged by electromagnetic induction surveys. *Geochemistry, Geophysics, Geosystems*, *15*(3), 509–515. https://doi.org/10.1002/2013GC004970

Bonner, L. R., & Schultz, A. (2017). Rapid prediction of electric fields associated with geomagnetically induced currents in the presence of three-dimensional ground structure: Projection of remote magnetic observatory data through magnetotelluric impedance tensors. *Space Weather*, *15*(1), 204–227. https://doi.org/10.1002/2016SW001535

Boteler, D. H. (1994). Geomagnetically induced currents: Present knowledge and future research. *IEEE Transactions on Power Delivery*, *9*(1), 50–58. https://doi.org/10.1109/61.277679

Boteler, D. H., & Pirjola, R. J. (2017). Modeling geomagnetically induced currents. *Space Weather*, *15*(1), 258–276. https://doi.org/10.1002/2016SW001499

Caraballo, R., Sánchez, L., & Tancredi, G. (2013). Geomagnetically induced currents in the Uruguayan high-voltage power grid. *Geophysical Journal International*, *195*(2), 844–853. https://doi.org/10.1093/gji/ggt293

Chave, A. D., & Jones, A. G. (2012). *The Magnetotelluric Method: Theory and Practice*. Cambridge, UK: Cambridge University Press. https://doi.org/10.1017/CBO9781139020138

Cherniak, I., & Zakharenkova, I. (2018). Large-scale traveling ionospheric disturbances origin and propagation: Case study of the December 2015 geomagnetic storm. *Space Weather*, *16*(9), 1377–1395. https://doi.org/10.1029/2018SW001869

Cuttler, S. W., Love, J. J., & Swidinsky, A. (2018). Geoelectric hazard assessment: The differences of geoelectric responses during magnetic storms within common physiographic zones. *Earth Planets and Space*, *70*(1), 35. https://doi.org/10.1186/s40623-018-0807-7

Denardini, C. M., Chen, S. S., Resende, L. C. A., Moro, J., Bilibio, A. V., Fagundes, P. R., et al. (2018). The embrace magnetometer network for South America: Network description and its qualification. *Radio Science*, *53*(3), 288–302. https://doi.org/10.1002/2017RS006477

Dimmock, A. P., Rosenqvist, L., Welling, D. T., Viljanen, A., Honkonen, I., Boynton, R. J., & Yordanova, E. (2020). On the regional variability of *dB*/*dt* and its significance to GIC. *Space Weather*, *18*(8), e2020SW002497. https://doi.org/10.1029/2020SW002497

Diogo, E. M. (2018). Modelagem de correntes geomagneticamente induzidas: Comparação de efeitos em diferentes latitudes (Doctoral dissertation, Instituto Nacional de Pesquisas Espaciais, São José dos Campos, Brazil). Retrieved from http://www.inpe.br/posgraduacao/ges/arquivos/teses/tese_erica_diogo_2018.pdf

Divett, T., Ingham, M., Beggan, C. D., Richardson, G. S., Rodger, C. J., Thomson, A. W. P., & Dalzell, M. (2017). Modeling geoelectric fields and geomagnetically induced currents around New Zealand to explore GIC in the South Island's electrical transmission network. *Space Weather*, *15*(10), 1396–1412. https://doi.org/10.1002/2017SW001697

Egbert, G. D., & Kelbert, A. (2012). Computational recipes for electromagnetic inverse problems. *Geophysical Journal International*, *189*(1), 251–267. https://doi.org/10.1111/j.1365-246X.2011.05347.x

Espinosa, K. V., Padilha, A. L., & Alves, L. R. (2019). Effects of ionospheric conductivity and ground conductance on geomagnetically induced currents during geomagnetic storms: Case studies at low-latitude and equatorial regions. *Space Weather*, *17*(2), 252–268. https://doi.org/10.1029/2018SW002094

Gannon, J. L., Birchfield, A. B., Shetye, K. S., & Overbye, T. J. (2017). A comparison of peak electric fields and GICs in the Pacific Northwest using 1-D and 3-D conductivity. *Space Weather*, *15*(11), 1535–1547. https://doi.org/10.1002/2017SW001677

Gaunt, C. T., & Coetzee, G. (2007). Transformer failures in regions incorrectly considered to have low GIC-risk. In *2007 IEEE Lausanne power Tech* (pp. 807–812). IEEE. https://doi.org/10.1109/PCT.2007.4538419

Grawe, M. A., Makela, J. J., Butala, M. D., & Kamalabadi, F. (2018). The impact of magnetic field temporal sampling on modeled surface electric fields. *Space Weather*, *16*(11), 1721–1739. https://doi.org/10.1029/2018SW001896

Heyns, M. J., Lotz, S. I., & Gaunt, C. T. (2021). Geomagnetic pulsations driving geomagnetically induced currents. *Space Weather*, *19*(2), e02557. https://doi.org/10.1029/2020SW002557

IEEE. (2007). *Grounding of Industrial and Commercial Power Systems* (142 edn.). Institute of Electrical and Electronics Engineers, Inc.

Kamide, Y., & Maltsev, Y. (2007). Geomagnetic storms. In Y. Kamide & A. Chian (Eds.), *Handbook of the solar-terrestrial environment* (pp. 355–374). Springer. https://doi.org/10.1007/978-3-540-46315-3_14

Kappenman, J. G. (2003). Storm sudden commencement events and the associated geomagnetically induced current risks to ground-based systems at low-latitude and midlatitude locations. *Space Weather*, *1*(3), 1016. https://doi.org/10.1029/2003SW000009

Kelbert, A. (2020). The role of global/regional Earth conductivity models in natural geomagnetic hazard mitigation. *Surveys in Geophysics*, *41*(1), 115–166. https://doi.org/10.1007/s10712-019-09579-z

Kelbert, A., Bedrosian, P. A., & Murphy, B. S. (2019). The first 3D conductivity model of the contiguous United States: Reflections on geologic structure and application to induction hazards. In J. L. Gannon, A. Swidinsky, & Z. Xu (Eds.), *Geomagnetically induced currents from the Sun to the power grid* (pp. 127–151). American Geophysical Union. https://doi.org/10.1002/9781119434412.ch8

Kelbert, A., & Lucas, G. M. (2020). Modified GIC estimation using 3-D Earth conductivity. *Space Weather*, *18*(8), e2020SW002467. https://doi.org/10.1029/2020SW002467

Kelbert, A., Meqbel, N., Egbert, G. D., & Tandon, K. (2014). Modem: A modular system for inversion of electromagnetic geophysical data. *Computers and Geosciences*, *66*, 40–53. https://doi.org/10.1016/j.cageo.2014.01.010

Lehtinen, M., & Pirjola, R. (1985). Currents produced in earthed conductor networks by geomagnetically-induced electric fields. *Annales Geophysicae*, *3*, 479–484.

Liu, Y. D., Hu, H., Wang, R., Yang, Z., Zhu, B., Liu, Y. A., et al. (2015). Plasma and magnetic field characteristics of solar coronal mass ejections in relation to geomagnetic storm intensity and variability. *The Astrophysical Journal*, *809*(2), L34. https://doi.org/10.1088/2041-8205/809/2/l34

Love, J. J., Lucas, G. M., Kelbert, A., & Bedrosian, P. A. (2018). Geoelectric hazard maps for the Pacific Northwest. *Space Weather*, *16*(8), 1114–1127. https://doi.org/10.1029/2018SW001844

Love, J. J., Lucas, G. M., Rigler, E. J., Murphy, B. S., Kelbert, A., & Bedrosian, P. A. (2022). Mapping a magnetic superstorm: March 1989 geoelectric hazards and impacts on United States power systems. *Space Weather*, *20*(5), e2021SW003030. https://doi.org/10.1029/2021SW003030

Lucas, G. M., Love, J. J., & Kelbert, A. (2018). Calculation of voltages in electric power transmission lines during historic geomagnetic storms: An investigation using realistic Earth impedances. *Space Weather*, *16*(2), 185–195. https://doi.org/10.1002/2017SW001779

Mantovani, M. S. M., Quintas, M. C. L., Shukowsky, W., & Brito Neves, B. B. (2005). Delimitation of the paranapanema proterozoic block: A geophysical contribution. *Episodes*, *28*(1), 18–22. https://doi.org/10.18814/epiiugs/2005/v28i1/002

Marshalko, E., Kruglyakov, M., Kuvshinov, A., Juusola, L., Kwagala, N. K., Sokolova, E., & Pilipenko, V. (2021). Comparing three approaches to the inducing source setting for the ground electromagnetic field modeling due to space weather events. *Space Weather*, *19*(2), e2020SW002657. https://doi.org/10.1029/2020SW002657

Marshall, R. A., Dalzell, M., Waters, C. L., Goldthorpe, P., & Smith, E. A. (2012). Geomagnetically induced currents in the New Zealand power network. *Space Weather*, *10*(8), S08003. https://doi.org/10.1029/2012SW000806

Marshall, R. A., Gorniak, H., Walt, T. V. D., Waters, C. L., Sciffer, M. D., Miller, M., et al. (2013). Observations of geomagnetically induced currents in the Australian power network. *Space Weather*, *11*(1), 6–16. https://doi.org/10.1029/2012SW000849

Maurya, V. P., Meju, M. A., Fontes, S. L., Padilha, A. L., La Terra, E. F., & Miquelutti, L. G. (2018). Deep resistivity structure of basalt-covered central part of Paraná Basin, Brazil, from joint 3-D MT and GDS data imaging. *Geochemistry, Geophysics, Geosystems*, *19*(7), 1994–2013. https://doi.org/10.1029/2017GC007314

McLay, S. A., & Beggan, C. D. (2010). Interpolation of externally-caused magnetic fields over large sparse arrays using Spherical Elementary Current Systems. *Annales Geophysicae*, *28*(9), 1795–1805. https://doi.org/10.5194/angeo-28-1795-2010

Melfi, A. J., Piccirillo, E. M., & Nardy, A. J. R. (1988). Geological and magmatic aspects of the Paraná Basin – An introduction. In E. M. Piccirillo & A. J. Melfi (Eds.), *The mesozoic flood volcanism of the Paraná basin* (pp. 1–13). IAG-USP.

Milani, E. J., & Ramos, V. A. (1998). Orogenias paleozóicas no domínio sul-ocidental do Gondwana e os ciclos de subsidência da Bacia do Paraná. *Revista Brasileira de Geociencias*, *28*(4), 473–484. https://doi.org/10.25249/0375-7536.1998473484

Murphy, B. S., Lucas, G. M., Love, J. J., Kelbert, A., Bedrosian, P. A., & Rigler, E. J. (2021). Magnetotelluric sampling and geoelectric hazard estimation: Are national-scale surveys sufficient? *Space Weather*, *19*(7), e2020SW002693. https://doi.org/10.1029/2020SW002693

Nakamura, S., Ebihara, Y., Fujita, S., Goto, T., Yamada, N., Watari, S., & Omura, Y. (2018). Time domain simulation of geomagnetically induced current (GIC) flowing in 500-kV power grid in Japan including a three-dimensional ground inhomogeneity. *Space Weather*, *16*(12), 1946–1959. https://doi.org/10.1029/2018SW002004

ONS. (2022). *SINDAT (Sistema de Informações Geográficas Cadastrais do SIN)*. Operador Nacional do Sistema Elétrico (ONS). https://sintegre.ons.org.br/sites/cadastro

Padilha, A. L., Vitorello, I., Antunes, C. E., & Pádua, M. B. (2015). Imaging three-dimensional crustal conductivity structures reflecting continental flood basalt effects hidden beneath thick intracratonic sedimentary basin. *Journal of Geophysical Research: Solid Earth*, *120*(7), 4702–4719. https://doi.org/10.1002/2014JB011657

Paulikas, G. A. (1975). Precipitation of particles at low and middle latitudes. *Reviews of Geophysics and Space Physics*, *13*(5), 709–734. https://doi.org/10.1029/RG013i005p00709

Pirjola, R. (2000). Geomagnetically induced currents during magnetic storms. *IEEE Transactions on Plasma Science*, *28*(6), 1867–1873. https://doi.org/10.1109/27.902215

Pirjola, R. (2002). Review on the calculation of surface electric and magnetic fields and of geomagnetically induced currents in ground-based technological systems. *Surveys in Geophysics*, *23*(1), 71–90. https://doi.org/10.1023/A:1014816009303

Pirjola, R., Viljanen, A., Pulkkinen, A., & Amm, O. (2000). Space weather risk in power systems and pipelines. *Physics and Chemistry of the Earth Part C*, *25*(4), 333–337. https://doi.org/10.1016/S1464-1917(00)00027-1

Pulkkinen, A., Amm, O., & Viljanen, A. (2003). Ionospheric equivalent current distributions determined with the method of spherical elementary current systems. *Journal of Geophysical Research*, *108*(A2), 1053. https://doi.org/10.1029/2001JA005085

Pulkkinen, A., Bernabeu, E., Eichner, J., Beggan, C., & Thomson, A. W. P. (2012). Generation of 100-year geomagnetically induced current scenarios. *Space Weather*, *10*(4), S04003. https://doi.org/10.1029/2011SW000750

Pulkkinen, A., Rastätter, L., Kuznetsova, M., Singer, H., Balch, C., Weimer, D., et al. (2013). Community-wide validation of geospace model ground magnetic field perturbation predictions to support model transition to operations. *Space Weather*, *11*(6), 369–385. https://doi.org/10.1002/swe.20056

Pulkkinen, A., Viljanen, A., & Pirjola, R. (2006). Estimation of geomagnetically induced current levels from different input data. *Space Weather*, *4*(8), S08005. https://doi.org/10.1029/2006SW000229

Rigler, E., Fiori, R., Pulkkinen, A., Wiltberger, M., & Balch, C. (2019). Interpolating geomagnetic observations: Techniques and comparisons. In J. L. Gannon, A. Swidinsky, & Z. Xu (Eds.), *Geomagnetically induced currents from the Sun to the power grid* (pp. 15–41). American Geophysical Union. https://doi.org/10.1002/9781119434412.ch2

Simpson, F., & Bahr, K. (2005). *Practical magnetotellurics*. Cambridge University Press. https://doi.org/10.1017/CBO9780511614095

Smith, S. W. (2013). *Digital signal processing: A practical guide for engineers and scientists*. Elsevier.

Sun, R., & Balch, C. (2019). Comparison between 1-D and 3-D geoelectric field methods to calculate geomagnetically induced currents: A case study. *IEEE Transactions on Power Delivery*, *34*(6), 2163–2172. https://doi.org/10.1109/TPWRD.2019.2905532

Torta, J. M., Marcuello, A., Campanyà, J., Marsal, S., Queralt, P., & Ledo, J. (2017). Improving the modeling of geomagnetically induced currents in Spain. *Space Weather*, *15*(5), 691–703. https://doi.org/10.1002/2017SW001628

Torta, J. M., Marsal, S., & Quintana, M. (2014). Assessing the hazard from geomagnetically induced currents to the entire high-voltage power network in Spain. *Earth Planets and Space*, *66*(1), 87. https://doi.org/10.1186/1880-5981-66-87

Torta, J. M., Serrano, L., Regué, J. R., Sánchez, A. M., & Roldán, E. (2012). Geomagnetically induced currents in a power grid of northeastern Spain. *Space Weather*, *10*(6), S06002. https://doi.org/10.1029/2012SW000793

Trichtchenko, L., & Boteler, D. H. (2006). Response of power systems to the temporal characteristics of geomagnetic storms. In *2006 Canadian conference on electrical and computer engineering* (pp. 390–393). IEEE. https://doi.org/10.1109/CCECE.2006.277733

Trivedi, N. B., Pathan, B. M., Schuch, N. J., Barreto, M., & Dutra, S. L. G. (2005). Geomagnetic phenomena in the South Atlantic anomaly region in Brazil. *Advances in Space Research*, *36*(10), 2021–2024. https://doi.org/10.1016/j.asr.2004.09.020

Trivedi, N. B., Vitorello, I., Kabata, W., Dutra, S. L. G., Padilha, A. L., Bologna, M. S., et al. (2007). Geomagnetically induced currents in an electric power transmission system at low latitudes in Brazil: A case study. *Space Weather*, *5*(4), 1–10. https://doi.org/10.1029/2006SW000282

Utada, H. (2018). *Plane-wave and flat Earth approximations in natural-source electromagnetic induction studies* (Vol. 93, pp. 1–14). Bulletin of the Earthquake Research Institute, University of Tokyo. https://doi.org/10.15083/0000051814

Vanhamäki, H., & Amm, O. (2011). Analysis of ionospheric electrodynamic parameters on mesoscales - a review of selected techniques using data from ground-based observation networks and satellites. *Annales Geophysicae*, *29*(3), 467–491. https://doi.org/10.5194/angeo-29-467-2011

Vanhamäki, H., & Juusola, L. (2020). Introduction to spherical elementary current systems. In M. W. Dunlop & H. Lühr (Eds.), *Ionospheric multi-spacecraft analysis tools: Approaches for deriving ionospheric parameters* (pp. 5–33). Springer. https://doi.org/10.1007/978-3-030-26732-2

Viljanen, A., Nevanlinna, H., Pajunpää, K., & Pulkkinen, A. (2001). Time derivative of the horizontal geomagnetic field as an activity indicator. *Annales Geophysicae*, *19*(9), 1107–1118. https://doi.org/10.5194/angeo-19-1107-2001

Viljanen, A., & Pirjola, R. (2017). Influence of spatial variations of the geoelectric field on geomagnetically induced currents. *Journal of Space Weather and Space Climate*, *7*, A22. https://doi.org/10.1051/swsc/2017024

Viljanen, A., Pirjola, R., Prácser, E., Ahmadzai, S., & Singh, V. (2013). Geomagnetically induced currents in Europe: Characteristics based on a local power grid model. *Space Weather*, *11*(10), 575–584. https://doi.org/10.1002/swe.20098

Wang, L., Duan, J., Hitchman, A. P., Lewis, A. M., & Jones, W. V. (2020). Modeling geoelectric fields induced by geomagnetic disturbances in 3D subsurface geology, an example from southeastern Australia. *Journal of Geophysical Research: Solid Earth*, *125*(9), e19843. https://doi.org/10.1029/2020JB019843

Watari, S., Kunitake, M., Kitamura, K., Hori, T., Kikuchi, T., Shiokawa, K., et al. (2009). Measurements of geomagnetically induced current in a power grid in Hokkaido, Japan. *Space Weather*, *7*(3), 03002. https://doi.org/10.1029/2008SW000417

Weigel, R. S. (2017). A comparison of methods for estimating the geoelectric field. *Space Weather*, *15*(2), 430–440. https://doi.org/10.1002/2016SW001504

Weygand, J. M., Amm, O., Viljanen, A., Angelopoulos, V., Murr, D., Engebretson, M. J., et al. (2011). Application and validation of the spherical elementary currents systems technique for deriving ionospheric equivalent currents with the North American and Greenland ground magnetometer arrays. *Journal of Geophysical Research*, *116*(3), A03305. https://doi.org.10.1029/2010JA016177

Zalán, P. V., Wolff, S., Astolfi, M. A. M., Vieira, I. S., Conceição, J. C. J., Appi, V. T., et al. (1990). The Paraná basin, Brazil. In M. W. Leighton, D. R. Kolata, D. F. Oltz, & J. J. Eidel (Eds.), *Interior cratonic basins* (pp. 681–708). American Association of Petroleum Geologists. https://doi.org/10.1306/M51530C34

Zheng, K., Boteler, D., Pirjola, R. J., Liu, L., Becker, R., Marti, L., et al. (2014). Effects of system characteristics on geomagnetically induced currents. *IEEE Transactions on Power Delivery*, *29*(2), 890–898. https://doi.org/10.1109/TPWRD.2013.2281191